

PVDIS Supplemental Material - Measurement of the
Parity Violating Deep Inelastic Asymmetry and
Extraction of the Quark Weak Axial Charge

D. Wang,¹ K. Pan,² R. Subedi,¹ X. Deng,¹ Z. Ahmed,⁴ K. Allada,⁵
 K. A. Aniol,⁶ D. S. Armstrong,⁷ J. Arrington,⁸ V. Bellini,⁹ R. Beminiwat
 J. Benesch,¹¹ F. Benmokhtar,¹² A. Camsonne,¹¹ M. Canan,¹³ G. D. Cat
 J.-P. Chen,¹¹ E. Chudakov,¹¹ E. Cisbani,¹⁴ M. M. Dalton,¹ C. W. de Jage
 R. De Leo,¹⁵ W. Deconinck,⁷ A. Deur,¹¹ C. Dutta,⁵ L. El Fassi,⁸ D. Fla
 G. B. Franklin,¹² M. Friend,¹² S. Frullani,¹⁴ F. Garibaldi,¹⁴ A. Giusa
 A. Glamazdin,¹⁷ S. Golge,¹³ K. Grimm,¹⁸ K. Hafidi,⁸ O. Hansen,¹¹ D. W. Hig
 R. Holmes,⁴ T. Holmstrom,¹⁹ R. Holt,⁸ J. Huang,² C. E. Hyde,^{13,20} C. M.
 D. Jones,¹ H. Kang,²¹ P. King,¹⁰ S. Kowalski,² K. S. Kumar,²² J. H. Lee
 J. J. LeRose,¹¹ N. Liyanage,¹ E. Long,²³ D. McNulty,²² D. Margaziotis,⁶ F.
 D. G. Meekins,¹¹ L. Mercado,²² Z.-E. Meziani,¹⁶ R. Michaels,¹¹ M. Mihov
 N. Muangma,² K. E. Myers,⁴ S. Nanda,¹¹ A. Narayan,²⁵ V. Nelyubin,¹ Nuruz
 Y. Oh,²¹ D. Parno,¹² K. D. Paschke,¹ S. K. Phillips,²⁶ X. Qian,²⁷
 Y. Qiang,²⁷ B. Quinn,¹² A. Rakhman,⁴ P. E. Reimer,⁸ K. Rider,¹⁹ S. Rior
 J. Roche,¹⁰ J. Rubin,⁸ G. Russo,⁹ K. Saenboonruang,¹ A. Saha,¹¹ †, B. Saw
 A. Shahinyan,¹¹ R. Silwal,¹ S. Sirca,²⁴ P. A. Souder,⁴ R. Suleiman,¹¹ V. Su
 C. M. Sutura,⁹ W. A. Tobias,¹ B. Waidyawansa,¹⁰ B. Wojtsekhowski,¹¹ L. Ye,²
 X. Zheng,^{1,*}

¹University of Virginia, Charlottesville, Virginia 22904, USA

²Massachusetts Institute of Technology, Cambridge, MA 02139, USA

³George Washington University, Washington, District of Columbia 20052, USA

⁴Syracuse University, Syracuse, New York 13244, USA

⁵University of Kentucky, Lexington, Kentucky 40506, USA

⁶California State University, Los Angeles, Los Angeles, California 90032, USA

⁷College of William and Mary, Williamsburg, Virginia 23187, USA

⁸Physics Division, Argonne National Laboratory, Argonne, Illinois 60439, USA

⁹Istituto Nazionale di Fisica Nucleare, Dipt. di Fisica dell'Univ. di Catania, I-95123 Cata

¹⁰Ohio University, Athens, Ohio 45701, USA

¹¹Thomas Jefferson National Accelerator Facility, Newport News, Virginia 23606, U

¹²Carnegie Mellon University, Pittsburgh, Pennsylvania 15213, USA

¹³Old Dominion University, Norfolk, Virginia 23529, USA

¹⁴INFN, Sezione di Roma, gruppo Sanità and Istituto Superiore di Sanità, I-00161 Rom

¹⁵Università di Bari, I-70126 Bari, Italy

¹⁶Temple University, Philadelphia, Pennsylvania 19122, USA

¹⁷Kharkov Institute of Physics and Technology, Kharkov 61108, Ukraine

¹⁸Louisiana Technical University, Ruston, Louisiana 71272, USA

¹⁹Longwood University, Farmville, Virginia 23909, USA

In this document we provide supplemental material in support of

Contents

1	PVDIS Formalism	5
2	Apparatus	6
2.1	Polarized Electron Beam	7
2.2	Beam Monitoring	9
2.3	Spectrometers and Detectors	12
2.3.1	Data Acquisition System	15
2.4	Beam Polarimetry	16
2.4.1	Mott Polarimeter	16
2.4.2	Møller Polarimeter	17
2.4.3	Compton Polarimeter	18
2.4.4	Beam Polarization Results	19
2.5	Target	21
2.6	Data Selection	22
2.7	Pedestals and Linearity	22
2.8	Systematic Fluctuations and Beam Corrections	26
2.9	Background Analysis	27
2.9.1	Charged Pion Background	28
2.9.2	Pair Production Background	30
2.9.3	Target EndCap Correction	31
2.9.4	Transverse Asymmetry Background	33
2.9.5	Target Purity, Density Fluctuation and Other False Asymmetries	35

2.10	Rescattering Background	36
2.11	Calibration of the HRS Optics	37
2.11.1	Hall Coordinate system (HCS)	38
2.11.2	Target Coordinate System (TCS)	38
2.11.3	Detector Coordinate System (DCS)	39
2.11.4	Transport coordinate System (TRCS)	39
2.11.5	VCD Timing Calibration	41
2.11.6	Beam Position Calibration	42
2.11.7	General Approach	44
2.11.8	Calibration Procedure	47
2.11.9	Optics Runlist Summary	47
2.11.10	Result	48
2.11.11	Q^2 Uncertainties	48
2.12	Reconstruction of Q^2 and x (HAMC)	58
2.13	Electromagnetic Radiative Correction	59
3	Extraction of Quark Axial Charge $2C_{2u} - C_{2d}$	70
3.1	Formalism and Structure Functions	70
3.2	Radiative Corrections	72
3.2.1	Running of all coupling constants	72
3.2.2	Box corrections	74
3.3	Extracting C_{2q}	76
3.4	The Higher Twist Effect and a Simultaneous Fit to the Higher Twist Coefficient β_{HT} and $2C_{2u} - C_{2d}$	78
4	Summary	79

1 PVDIS Formalism

This section discusses the formalism of parity-violating deep inelastic scattering. Extraction of the C_2 coefficients (section 3) follow from this formalism.

$$A_{PV} \equiv \frac{\sigma_+ - \sigma_-}{\sigma_+ + \sigma_-} = \left(-\frac{G_F Q^2}{4\sqrt{2}\pi\alpha} \right) \left(2g_A^e Y_1 \frac{F_1^{\gamma Z}}{F_1^\gamma} + g_V^e Y_3 \frac{F_3^{\gamma Z}}{F_1^\gamma} \right), \quad (1)$$

where Q^2 is the negative of the four-momentum transfer squared, G_F is the Fermi weak coupling constant, α is the fine structure constant, Y_1 and Y_3 are kinematic factors, and x is the Bjorken scaling variable. In the quark parton model,

$$F_1^{\gamma Z} = \sum g_V^q Q_q [q(x) + \bar{q}(x)] \quad (2)$$

$$F_3^{\gamma Z} = \sum g_A^q Q_q [q(x) - \bar{q}(x)] \quad (3)$$

$$F_1^\gamma = \frac{1}{2} \sum Q_q^2 [q(x) + \bar{q}(x)] \quad (4)$$

where Q_q is the electric charge of quarks and $q(x)$, $\bar{q}(x)$ are quark distribution functions. Rewriting $g_{A(V)}^e g_{V(A)}^q$ as $C_{1(2)q}$, and assuming $R^\gamma = R^{\gamma Z} = 0$, one has $Y_1 = 1$ and

$$A_{PV} = \left(\frac{3G_F Q^2}{\pi\alpha^2\sqrt{2}} \right) \times \frac{2C_{1u}[1 + R_C(x)] - C_{1d}[1 + R_S(x)] + Y_3(2C_{2u} - C_{2d})R_V(x)}{5 + R_S(x) + 4R_C(x)}, \quad (5)$$

where $R_{V,C,S}$ are related to quark distributions. The magnitude of the asymmetry is in the order of 10^{-4} , or 10^2 parts per million (ppm) at $Q^2 = 1 \text{ (GeV/c)}^2$.

The tree-level Standard Model effective weak coupling constants $C_{1,2q}$ are

$$\begin{aligned} C_{1u} &= 2g_A^e g_V^u = -\frac{1}{2} + \frac{3}{4} \sin^2 \theta_W, & C_{2u} &= 2g_V^e g_A^u = -\frac{1}{2} + 2 \sin^2 \theta_W, \\ C_{1d} &= 2g_A^e g_V^d = \frac{1}{2} - \frac{2}{3} \sin^2 \theta_W, & C_{2d} &= 2g_V^e g_A^d = \frac{1}{2} - 2 \sin^2 \theta_W, \end{aligned}$$

with θ_W the weak mixing angle. The goal of JLab E08-011 is to measure the PVDIS asymmetries to a statistical precision of 3% for the $Q^2 = 1.1\text{GeV}^2$ point and 4% for the $Q^2 = 1.9\text{GeV}^2$ point. In addition, the systematic uncertainty goal is $< 3\%$, and under the assumption that hadronic physics corrections are small, our goal is to extract from these asymmetries the effective coupling constant combination $(2C_{2u} - C_{2d})$. The magnitude of the asymmetries is expected to be 90 and 170 ppm for the two measured kinematics of $Q^2 = 1.1$ and $1.9 (\text{GeV}/c)^2$, respectively. To achieve the required precision, event rates up to 500 kHz are expected. Although this is not the first time the PVDIS asymmetries are measured, the only preceeding PVDIS measurement was carried out at SLAC (3) about 35 years ago, with a $\approx 9\%$ statistical and a $\approx 9\%$ systematic uncertainties. The increased precision of this experiment required better controls of all systematic uncertainties.

2 Apparatus

The floor plan for Hall A is shown in figure 1. We used an $85 \mu\text{A}$ polarized electron beam and a 25 cm liquid deuterium target. The scattered electrons are detected by the two High Resolution Spectrometers (HRS) in Hall A at Jefferson Lab. A Luminosity Monitor is located downstream on the beamline to monitor the target boiling effects and possible false asymmetries at the 10^{-7} level.

The experimental techniques for measuring small asymmetries of order 1 ppm have been successfully deployed in parity-violating electron-scattering experiments at several facilities (3–8). The recent experiments at Jefferson Lab, such as HAPPEX (6) and PREX (8) have maintained systematic uncertainties associated with helicity reversal at the 10^{-8} level. The asymmetries sought for in this experiment are of order 100 ppm with required accuracies of about 1 ppm, which is two orders-of-magnitude above the systematic uncertainty established in the recent experiments.

The measurement must separate electrons from the charged pion background that arise from electro- or photo-production. While the standard HRS detector package and data acquisition (DAQ) system routinely provide such a high particle identification (PID) performance, they are based on full recording of the detector signals and are limited to event rates up to 4 kHz. This is not sufficient for the few-hundred kHz rates for the experiment. Thus we have built new DAQ designed to count event rates up to 1 MHz with hardware-based particle identification (see Ref. (9) and section 2.3.1).

The apparatus will be described in detail in this section. These include the polarized electron beam (section 2.1), the beam monitors (2.2), the spectrometers and detectors(2.3), the data acquisition system (2.3.1, the target (2.5), and the beam polarimeters (2.4).

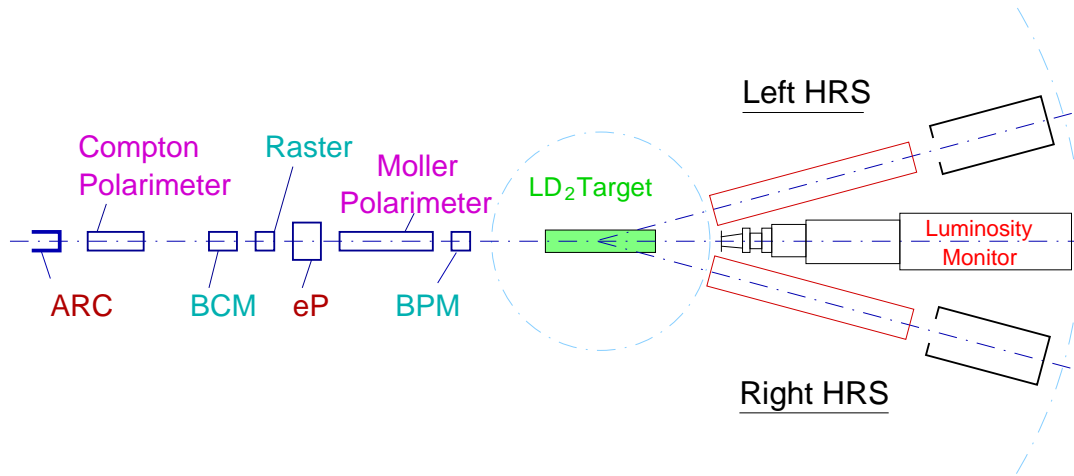


Figure 1: Floor plan of the PVDIS experiment in Hall A at Jefferson Lab. Beam enters from the left and scatters from a LD_2 target in the middle of the hall. The scattered electrons are detected in the two HRS (High Resolution Spectrometer) systems.

2.1 Polarized Electron Beam

The electron beam originated from a strained GaAsP photocathode illuminated by circularly polarized light (10). The sign of the laser polarization determined the electron helicity; this was held constant for periods of 33 msec, referred to as “windows”. By reversing the sign of the laser

circular polarization, the direction of the spin at the target could be reversed rapidly (11). Two windows of opposite helicity made a window pair, where the helicity of the first window was chosen with a pseudorandom number generator and the second window was the complement. These window pairs were line locked to the 60 Hz line, thus ensuring a good cancellation of the power-line noise.

A half-wave ($\lambda/2$) plate was periodically inserted into the laser optical path which passively reversed the sign of the electron beam polarization. Roughly equal statistics were thus accumulated with opposite signs for the measured asymmetry, which suppressed many systematic effects. The direction of the polarization could also be controlled by a Wien filter and solenoidal lenses near the injector (12). The accelerated beam was directed into Hall A, where its intensity, energy and trajectory on target were inferred from the response of several monitoring devices.

The beam monitors and trigger signals, which derived from the detectors in the spectrometers, were integrated over the helicity window and digitized. The beam monitors were integrated by custom 18-bit ADCs (8), see section 2.3.1. The beam monitors, target, and detectors were designed so that the fluctuations in the fractional difference in the signal response between a pair of successive windows were dominated by scattered electron counting statistics (see sec 2.8). To keep spurious beam-induced asymmetries under control at well below the ppm level, careful attention was given to the design and configuration of the laser optics leading to the photocathode (11).

The integrated response of each detector PMT and beam monitor was digitized and recorded for each 33 msec window. The raw spin-direction asymmetry A_{raw} in each spectrometer arm was computed from the the detector response normalized to the beam intensity for each window pair.

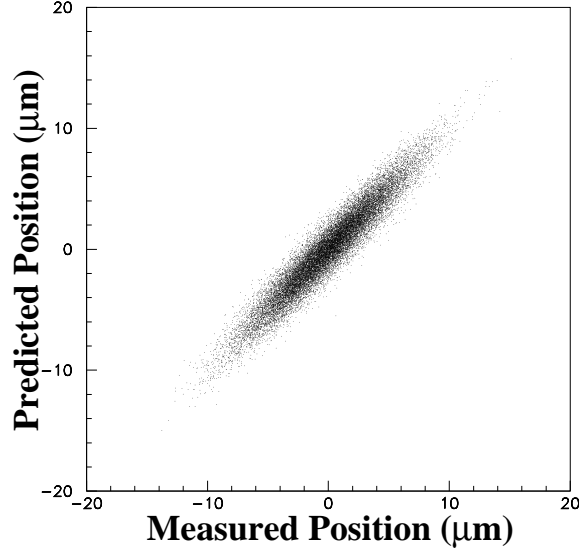


Figure 2: Window-to-window beam jitter as measured by a BPM is plotted along the x axis. On the y axis is plotted the beam position as predicted by nearby BPMs. The residuals are smaller than $1 \mu\text{m}$.

2.2 Beam Monitoring

Helicity-correlations in the beam properties such as energy and position are a primary concern for parity-violation experiments. At Jefferson Lab, the beam position is measured by “stripline” monitors (13), each of which consists of a set of four thin wires placed symmetrically around the beam pipe. The wires act as antennae that provide a signal (modulated by the microwave structure of the electron beam) proportional to the beam position as well as intensity. Figure 2 shows the correlation between the measured position at a BPM near the target compared with the predicted position using neighboring BPMs for a beam current of $100 \mu\text{A}$ (2×10^{13} electrons per window). A precision for $\delta(\Delta X_i)$ close to $1 \mu\text{m}$ was obtained for the average beam position for a beam window containing 2×10^{13} electrons.

To measure the beam intensity, microwave cavity BCMs have been developed at Jefferson Lab (14). The precision $\delta(A_I)$ that has been achieved for a 30 ms beam window at 100 μA is 4×10^{-5} . This resolution is a result of good radiofrequency (rf) instrumentation as well as a high resolution of the 18-bit ADC (sec 2.3.1).

Let the detected scattered flux of electrons be D in each spectrometer, and the beam current I , measured independently for every window by integrating the signals over the helicity period. From these we obtained the normalized flux $d_i \equiv D_i/I_i$ and the cross section asymmetry $(A_d)_i$ for the i th window pair. The raw asymmetry was then obtained by appropriate averaging of N measurements:

$$\begin{aligned} (A_d)_i &\equiv \left(\frac{d^+ - d^-}{d^+ + d^-} \right)_i \equiv \left(\frac{\Delta d}{2d} \right)_i \\ \delta(A_d) &= \sigma(A_d)/\sqrt{N}. \end{aligned} \tag{6}$$

where $+$ and $-$ denote the two helicity states in a pair.

A major goal of the experimental design is to $\sigma(A_d)$ should be dominated by the counting statistics in the scattered flux. As shown by fig 10 in Ref. (9), this goal was met.

There are two key parameters for each experimentally measured quantity M , such as detector rate, beam intensity, or beam position. The first is $\sigma(\Delta M)$, the size of the relative window pair-to-window pair fluctuations in $\Delta M \equiv M_+ - M_-$, which is affected by real fluctuations in the electron flux. The second is $\delta(\Delta M)$, the relative accuracy with which the window pair differences in M can be measured compared to the true value, which is dominated by instrumentation noise.

If $\sigma(\Delta M)$ is large enough, it might mean that there are non-statistical contributions to $\sigma(A_d)$ so that the latter is no longer dominated by counting statistics. In this case, it is important that $\delta(\Delta M) \ll \sigma(\Delta M)$ so that window pair to window pair corrections for the fluctuations in ΔM can be made.

We desire that $\sigma(A_d)$ be dominated by counting statistics; this minimizes the run time and demonstrates that we know the main source of our uncertainties. An example of possible non-statistical contributions is window-to-window relative beam intensity fluctuations, $\sigma(A_I) \equiv \sigma(\Delta I/2I)$, which were observed to vary between 2×10^{-4} and 2×10^{-3} , depending on the quality of the laser and the beam tune. This is a unique strength of the beam at Jefferson lab, since $\sigma(A_I) < \sigma(A_d)$. Nevertheless, the detector-intensity correlation can be exploited to remove the dependence of beam charge fluctuations on the measured asymmetry:

$$(A_d)_i \simeq \left(\frac{\Delta D}{2D} - \frac{\Delta I}{2I} \right)_i \equiv (A_D - A_I)_i. \quad (7)$$

which is equation 6 to first order.

Similarly, $\sigma(A_d)$ might be affected by random beam fluctuations in energy, position and angle. The corrections can be parameterized as follows:

$$(A_d^{\text{corr}})_i = \left(\frac{\Delta D}{2D} - \frac{\Delta I}{2I} \right)_i - \sum_j (\alpha_j (\Delta X_j)_i). \quad (8)$$

Here, X_j are beam parameters such as energy, position and angle and $\alpha_j \equiv \partial D / \partial X_j$ are coefficients that depend on the kinematics of the specific reaction being studied, as well as the detailed spectrometer and detector geometry of the experiment.

With a careful choice of beam position monitoring devices (BPMs) and their respective locations, several measurements of beam position can be made from which the average relative energy, position, and angle of approach of each ensemble of electrons in a helicity window on target can be inferred. One can then write

$$(A_d^{\text{corr}})_i = \left(\frac{\Delta D}{2D} - \frac{\Delta I}{2I} \right)_i - \sum_j (\beta_j (\Delta M_j)_i). \quad (9)$$

Here M_i are a set of 5 BPMs that span the parameter space of energy, position, and angle on target, and $\beta_i \equiv \partial D / \partial M_i$. It is worth noting that this approach of making corrections window

by window automatically accounts for occasional random instabilities in the accelerator (such as klystron failures) that are characteristic of normal running conditions.

During our experiment run, we found that $\sigma(\Delta M_j)$ varied between 1 and 10 μm and $\sigma(A_E)$ was typically less than 10^{-5} . These fluctuations were small enough that their impact on $\sigma(A_d)$ was negligible.

The coefficients β_i were evaluated using beam modulation, and will be discussed in Sect. 2.8, where it is shown that the corrections were negligible compared to the uncertainties from counting statistics.

2.3 Spectrometers and Detectors

The Hall A high resolution spectrometers (HRS) at Jefferson Lab consist of a pair of identical spectrometers of QQDQ design, together with detectors for detecting the scattered particles (14). The spectrometer and their standard detector package served to select for and to measure the kinematics quantities (x, Q^2) while suppressing backgrounds originating from the target.

The spectrometers are designed to have a large acceptance with excellent resolution ($\Delta E/E \sim 10^{-4}$) and absolute accuracy in the reconstructed four-vectors of the events and, of less relevance for our experiment, precise normalization of the cross section. To measure Q^2 with sufficient accuracy requires good knowledge of the transfer matrix for the spectrometer to reconstruct events at the scattering point, as well as good pointing accuracy for the location of the spectrometers and precise measurements of beam position and angle. To calibrate the transfer matrix, a 0.5 mm thick tungsten plate with an array of pinholes is inserted in dedicated runs; reconstruction of the hole pattern determines the matrix.

The scattered rate of electrons and of pions were determined by a trigger system in the HRS described in (9). This trigger consisted of two scintillator planes, which provided the main timing trigger, a CO_2 gas cherenkov counter and a double-layered lead glass detector, which

both provided particle identification information. The standard tracking detector (the vertical drift chamber) was turned off during production data taking because it may not endure the expected high event rates. During low-rate calibration runs, the tracking detector was turned on and the efficiency of the electron trigger and the pion rejection could be studied (see Ref. (9)).

The signals for the gas cherenkov detector and the double-layered lead glass counter were passed through discriminators and logic units to form preliminary electron and pion triggers. These preliminary triggers are then combined with the scintillator triggers and cherenkov signals to form the final electron and pion triggers, which are then sent to scalers to record the event counts and form asymmetries. Particle identification is fulfilled by the use of discriminators for both the lead-glass and the cherenkov counters and proper settings of their thresholds.

For HRS the two layers of the leadglass counter are called “preshower” and “shower” detectors, respectively. The preshower blocks in the Right HRS (the spectrometer located to the right side of the beamline when viewed along the beam direction) has 48 blocks arranged in a 2×24 array, with the longest dimension of the blocks aligned perpendicular to the particle trajectory. For the two blocks in each row, only the ends facing outward are read out by photomultiplier tubes (PMTs) and the other ends of the two blocks were facing each other and not read out. Therefore the preshower detector had 48 output channels. All preshower blocks were individually wrapped to prevent light leak. The preshower and the shower detectors in the Left HRS are similar to the preshower detector on the Right HRS except that for each detector there are 34 blocks arranged in a 2×17 array. The shower detector in the Right HRS had 75 blocks arranged in a 5×15 array with the longest dimension of the blocks aligned along the trajectory of scattered particles. PMTs are attached to each block of the Right shower detector on one end only, giving 75 output channels.

The particle identification (PID) was studied at low beam currents using fbTDC signals along with ADC spectrum of all detector signals recorded by the standard DAQ. Figure 3 shows

the preshower vs. shower signals for group 2 on the Left HRS. A comparison between no fbTDC cut and with cut on the fbTDC signal of the electron wide trigger from this group clearly shows the hardware PID cuts.

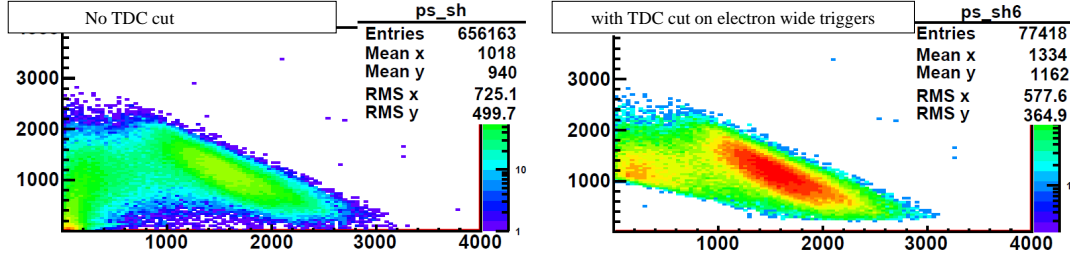


Figure 3: Preshower vs. Shower ADC spectrum (sum of 8 blocks each) for group 2 on the Left HRS, without fbTDC cut (left) and with cut on the group 2 electron wide trigger fbTDC signal (right). It clearly shows the hardware cuts on the preshower and the total shower signals, indicating the DAQ is selecting the correct events as electrons. The cuts can be adjusted by changing the discriminator thresholds. The events near the vertical axis, around ADC channels (200,1000), are electrons that deposited energy in overlapping blocks between group 2 and group 1 (or group 3) and are recorded by the other group.

Electron efficiency and pion rejection factors of the lead glass counter on the Left HRS are shown in Fig. 4 as functions of the vertical hit position of the particle in the preshower detector. PID performance on the Right HRS is similar. Electron efficiency from wide groups are slightly higher than narrow groups because there is less event loss due to timing mis-alignment when taking the coincidence between the preshower and the total shower discriminator outputs. Variations in the electron efficiency across the spectrometer acceptance effectively change the kinematics (Q^2) of the measurement. For this reason, data were taken daily during the experiment to monitor the DAQ PID performance and corrections are applied to data.

Combined with the ≈ 200 pion rejection factor of the gas cherenkov counter, the total pion rejection was above 10^4 . With the parity violation asymmetry of pion production being no larger than that of scattered electrons, the uncertainty in the final asymmetry results due to pion contamination is negligible compared to the 3 – 4% statistical uncertainty.

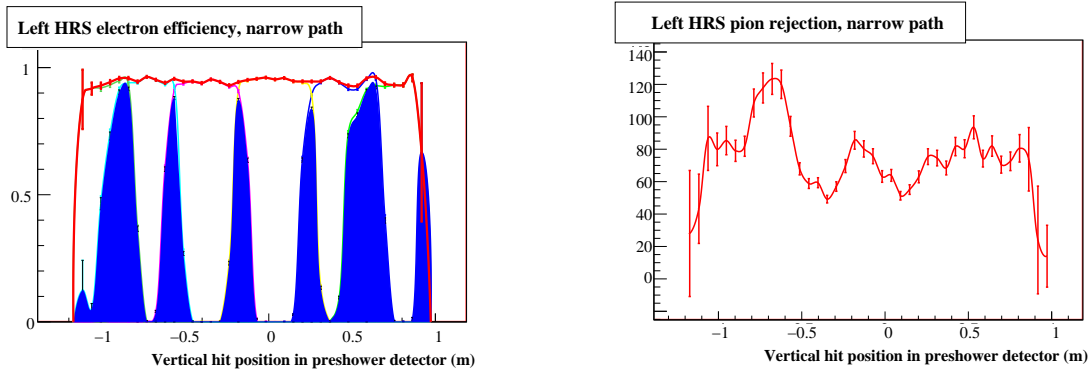


Figure 4: Electron detection efficiency (left) and pion rejection factor (right) vs. vertical (dispersive) hit position of the particle in the preshower detector for the narrow electron triggers in the Left HRS. A one-hour run was used in this evaluation. For electron efficiencies, the total efficiency is shown by the red curve, while blue shaded area indicates events that are recorded by the two adjacent groups. The average electron efficiency across the detector for this one-hour run is $(94.626 \pm 0.002)\%$ and the average pion rejection factor is 75.3 ± 1.1 . The error bars are statistical only. PID performance for the wide path and the Right HRS are similar.

2.3.1 Data Acquisition System

The signals from our trigger that define electrons and pions are sent to scalers (Struck Model SIS3801) where they are integrated over the helicity window. The scalers are part of the HAPPEX DAQ (6) which is a multiple-VME-crate DAQ system running under the CODA system developed at Jefferson Lab (15). Signals from the various beam monitors are integrated and digitized by custom-built VME integrating 18-bit ADCs. The system is triggered at the 30 Hz rate of the helicity reversal, synchronized to the end of each helicity window with the first 0.5 msec of the pulse blanked off to remove instabilities due to the switching of HV on the Pockels cell which controls the beam polarization. In addition to the scalers and ADCs, the DAQ reads input/output registers which record various information such as the helicity.

The scaler DAQ which counts triggers is designed to count event rates up to 1 MHz with hardware-based PID and with minimal deadtime of order 1%. The analysis of the deadtime is given in reference (9). The detectors (section 2.3) provided the electron and pion triggers. A

schematic and full description of the trigger is shown in ref (9).

2.4 Beam Polarimetry

The experimental asymmetry A^{exp} is related to the corrected asymmetry by

$$A^{\text{exp}} = A_d^{\text{corr}} / P_e \quad (10)$$

where P_e is the beam polarization. Three beam polarimetry techniques were available at JLab: A Mott polarimeter in the injector, and both a Møller and a Compton polarimeter in the experimental hall.

2.4.1 Mott Polarimeter

A Mott polarimeter (16) is located near the injector to the first linac, where the electrons have reached 5 MeV in energy. Mott polarimetry is based on the scattering of polarized electrons from unpolarized high-Z nuclei. The spin-orbit interaction of the electron's spin with the magnetic field it sees due to its motion relative to the nucleus causes a differential cross section

$$\sigma(\theta) = I(\theta) \left[1 + S(\theta) \vec{P}_e \cdot \hat{n} \right] , \quad (11)$$

where $S(\theta)$ is the Sherman function and $I(\theta)$ is the spin-averaged scattered intensity

$$I(\theta) = \frac{Z^2 e^4}{4m^2 \beta^4 c^4 \sin^4(\theta/2)} \left[1 - \beta^2 \sin^2(\theta/2) \right] (1 - \beta^2) . \quad (12)$$

The unit vector \hat{n} is normal to the scattering plane, defined by $\hat{n} = (\vec{k} \times \vec{k}') / |\vec{k} \times \vec{k}'|$ where \vec{k} and \vec{k}' are the electron's momentum before and after scattering, respectively. Thus $\sigma(\theta)$ depends on the electron beam polarization P_e . Defining an asymmetry

$$A(\theta) = \frac{N_L - N_R}{N_L + N_R} , \quad (13)$$

where N_L and N_R are the number of electrons scattered to the left and right, respectively, we have

$$A(\theta) = P_e S(\theta), \quad (14)$$

and so knowledge of the Sherman function $S(\theta)$ allows P_e to be extracted from the measured asymmetry with a precision of 3% (6, 17). The Mott polarimeter is also used for setting up and verifying the transversely-polarized beam used for systematic checks.

2.4.2 Møller Polarimeter

A Møller polarimeter measures the beam polarization via measuring the asymmetry in \vec{e}, \vec{e}' scattering, which depends on the beam and target polarizations P^{beam} and P^{target} , as well as on the analyzing power A_m^{th} of Møller scattering:

$$A_m^{\text{exp}} = \sum_{i=X,Y,Z} (A_{mi}^{\text{th}} \cdot P_i^{\text{targ}} \cdot P_i^{\text{beam}}), \quad (15)$$

where $i = X, Y, Z$ defines the projections of the polarizations (Z is parallel to the beam, while $X - Z$ is the scattering plane). The analyzing powers A_{mi}^{th} depend on the scattering angle θ_{CM} in the center-of-mass (CM) frame and are calculable in QED. The longitudinal analyzing power is

$$A_{mZ}^{\text{th}} = -\frac{\sin^2 \theta_{\text{CM}} (7 + \cos^2 \theta_{\text{CM}})}{(3 + \cos^2 \theta_{\text{CM}})^2}. \quad (16)$$

The absolute values of A_{mZ}^{th} reach the maximum of 7/9 at $\theta_{\text{CM}} = 90^\circ$. At this angle the transverse analyzing powers are $A_{mX}^{\text{th}} = -A_{mY}^{\text{th}} = A_{mZ}^{\text{th}}/7$.

The polarimeter target is a ferromagnetic foil magnetized in a magnetic field of 24 mT along its plane. The target foil can be oriented at various angles in the horizontal plane providing both longitudinal and transverse polarization measurements. The asymmetry is measured at two target angles ($\pm 20^\circ$) and the average taken, which cancels transverse contributions and reduces the uncertainties of target angle measurements. At a given target angle two sets of measurements

with oppositely signed target polarization are made which cancels some false asymmetries such as beam current asymmetries. The target polarization was $(7.95 \pm 0.24)\%$.

The Møller-scattered electrons were detected in a magnetic spectrometer consisting of three quadrupoles and a dipole (14). The spectrometer selects electrons in a bite of $75^\circ \leq \theta_{\text{CM}} \leq 105^\circ$ and $-5^\circ \leq \phi_{\text{CM}} \leq 5^\circ$ where ϕ_{CM} is the azimuthal angle. The detector consists of lead-glass calorimeter modules in two arms to detect the electrons in coincidence. More details about the Møller polarimeter are published in (14). The total systematic error that can be achieved is 3.2% which is dominated by uncertainty in the foil polarization.

2.4.3 Compton Polarimeter

The Compton polarimeter (18–20) is based on scattering of the polarized electron beam from a polarized laser in a beam chicane. The backscattered photons are detected in a GsO crystal (20).

The experimental asymmetry $A_c^{\text{exp}} = (N^+ - N^-)/(N^+ + N^-)$ is measured, where N^+ (N^-) refers to Compton counting rates for right (left) electron helicity, normalized to the beam intensity. This asymmetry is related to the electron beam polarization via

$$P_e = \frac{A_c^{\text{exp}}}{P_\gamma A_c^{\text{th}}} \quad (17)$$

where P_γ is the photon polarization and A_c^{th} the analyzing power. At typical JLab energies (a few GeV), the Compton cross-section asymmetry is only a few percent. To compensate for this, a Fabry-Perot cavity (21) is used to amplify the photon density of a standard low-power laser at the integration point. An average power of 1200 W is accumulated inside the cavity with a photon beam waist of the order of 150 μm and a photon polarization above 99%, monitored online at the exit of the cavity (22).

2.4.4 Beam Polarization Results

During our experimental run, the Møller polarimeter the entire time, while the Compton polarimeter initially suffered from a high background and only produced results in the last three weeks of the run. Figure 5 shows the Møller polarimetry measurements during our experiment, and figure 6 shows the Compton measurements together with Møller measurements that were taken during the time period.

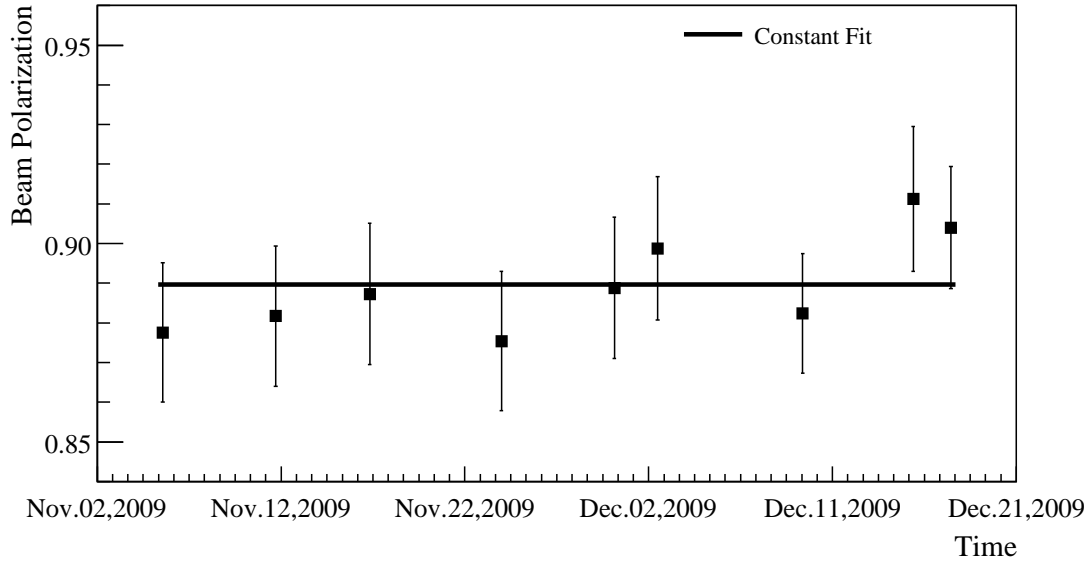


Figure 5: Polarization history from the Møller polarimeter measurements. The error bars include systematic error.

The average beam polarization from constant fit is 88.97% for Møller and 89.45% for Compton. The way that we apply the beam polarization correction is as following:

1. When there's no Compton measurements (before Dec 2), only Møller results are used. Each Moller data point is used for the consecutive days until the next data point is available.

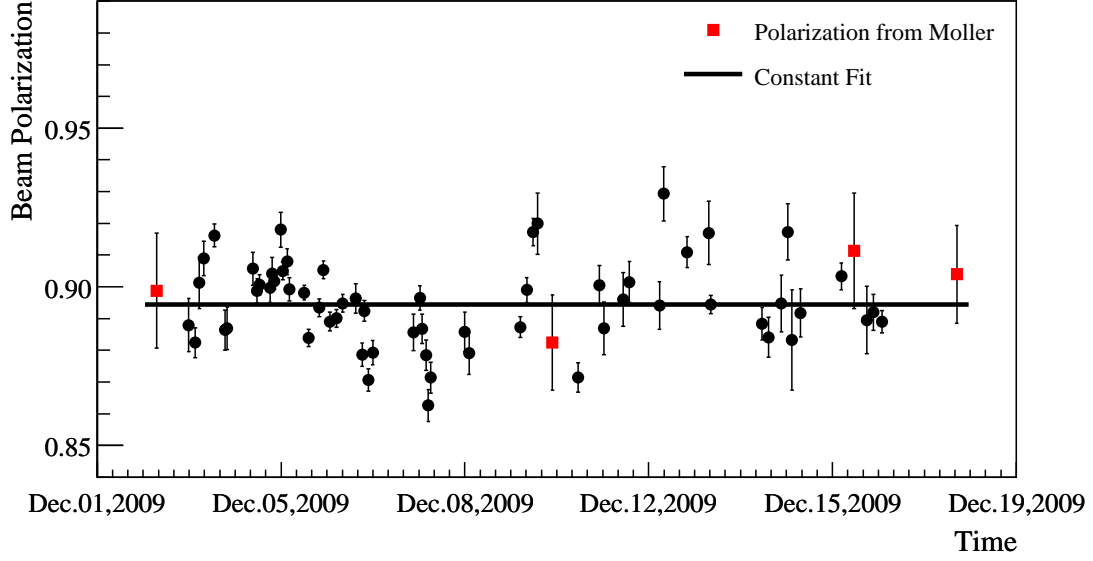


Figure 6: Polarization history from Compton measurement (round points), together with Moller measurements (square points) during the same time. The error bars for Compton are statistical only, while for Moller include systematic.

2. When there are both Compton and Møller results (after Dec 2), the Compton data are averaged first and then this average is averaged with each Moller point. These results are applied for correction in the same way as 1.
3. The beam polariztion is corrected run by run.

The run-by-run averaged beam polarization corrections are shown in table 2.4.4 for the different kinematics and spectrometers (Left/Right HRS).

	Left Kine 1	Left Kine 2	Right Kine 2
Polarization	88.18%	89.29%	88.73%
Uncertainty	1.76%	1.19%	1.50%

2.5 Target

The Hall A cryogenic target system (14) was used for this experiment. We used the a 20 cm deuterium cylindrical target cell for the main production data-taking, as well as auxiliary targets for evaluating backgrounds, studying the spectrometer optics, and checking beam centering. The target cell sits in an evacuated scattering chamber, along with subsystems for cooling, temperature and pressure monitoring, target motion, gas-handling, controls, and a solid and dummy target ladder.

The liquid deuterium loop was operated at a temperature of 22 K and a pressure of 25 psia, leading to a density of about 0.0723 g/cm^3 . The Al-walled target cells were 6.48 cm in diameter, and were oriented horizontally, along the beam direction. The upstream window thickness was 0.071 mm, the downstream window thickness was 0.094 mm, and the side wall thickness was 0.18 mm. Also mounted on the target ladder were solid thin targets of carbon, and aluminum dummy target cells, for use in background and spectrometer studies.

The target was mounted in a cylindrical scattering chamber of 104 cm diameter, centered on the pivot for the spectrometers. The scattering chamber was maintained under a 10^{-6} torr vacuum. The spectrometers view exit windows in the scattering chamber that were made of 0.406 mm thick Al foil.

To spread the heat load on the the target end-cap, the beam was rastered at 20 kHz by two sets of steering magnets 23 m upstream of the target. These magnets deflected the beam by up to ± 2.5 mm in x and y at the target. Local target boiling would manifest itself as an increase in fluctuations in the measured scattering rate, which would lead to an increase in the standard deviation of the pulse-pair asymmetries in the data, above that expected from counting statistics. Studies of the pulse-pair asymmetries for various beam currents and raster sizes were performed, at a lower Q^2 and thus at a higher scattering rate. Figure ?? shows the standard deviation of the pulse-pair asymmetries, extrapolated to full current values, for various beam

currents and raster sizes. A significant increase over pure counting statistics, indicating local boiling effects, was observed only for the combination of a small raster (1.0 mm) size and large beam current (94 μA). During the experiment we used larger raster sizes for which there was negligible boiling noise.

2.6 Data Selection

Loose requirements were imposed on beam quality, removing periods of beam intensity, position, or energy instability, removing about 25% of the total data sample. No spin-direction-dependent cuts were applied. The dominant source of noise due to the beam arose from fluctuations in the beam current and beam energy.

As explained in detail in (8, 23, 24), the window-to-window differences in the asymmetry from beam jitter were reduced by using the correlations to beam position differences from precision beam position monitors, Δx_i by defining a correction $A_{beam} = \sum c_i \Delta x_i$. The c_i were measured several times each hour from calibration data where the beam was modulated using steering coils and an accelerating cavity. The largest c_i was for ^{208}Pb and was on the order of 50 ppb/nm. The spread in the resulting $A_n^m = A_{raw} - A_{beam}$ was observed to be dominated by counting statistics.

2.7 Pedestals and Linearity

The signals produced by the beam monitors and the detectors ideally are proportional to the actual rates in those devices. In reality, however, these signals can deviate from linearity over the full dynamic range and in general do not extrapolate to a zero pedestal.

To study the linearity of the detectors and cavity monitors, we compared them to an Unser monitor (25), a parametric current transformer which can be used as an absolute reference of current. For our purposes the Unser monitor's advantage is its excellent linearity at low

currents which allows us to obtain the cavity monitor pedestals. However, the fluctuations in the Unser monitor's pedestals, which drift significantly on a time scale of several minutes, and the ordinarily small range of beam currents limited the precision of such comparisons during production data taking. Instead, we use calibration data in which the beam current is ramped up and down from zero to more than $50 \mu\text{A}$. One cycle takes about a minute. The result is that for any given beam current we have about sixty samples spread over a half hour run. This breaks any random correlation between Unser pedestal fluctuations and beam current and converts the Unser pedestal systematic to a random error.

In order to study linearity, we make scatterplots of one signal versus another and fit each scatterplot to a straight line, using only events where $24 \mu\text{A} < I_1 < 34 \mu\text{A}$, a range in which exploratory fits suggested everything was fairly linear. We then examine the residuals between the scatterplots and the fits, relative to the signal size corresponding to about $32 \mu\text{A}$, over the full range of beam current.

Figures 7 to 8 show the results as a function of I_1 . In Fig. 7 we see the behavior of the two cavity monitors relative to the Unser monitor. Both show deviations from linearity below about $14 \mu\text{A}$ and above about $47 \mu\text{A}$, though the high-current problem for I_1 is not as clear-cut as for I_2 and the nonlinearities are at worst about 1% of the signal.

In Fig. 8 we see residuals for fits of the two detector signals versus I_1 . The nonlinear behavior at low current is due mainly to the cavity monitors. From $32 \mu\text{A}$ to over $50 \mu\text{A}$ the detectors are linear to well under 0.2%.

We may conclude that the detectors and cavity monitors are linear to well within the required tolerances.

Detector pedestals were measured by averaging the detector signals during times when the beam is off. The resulting pedestals were always less than 0.3% of the signal corresponding to the lowest stable beam current in the production data set, and typically less than 0.06%; these

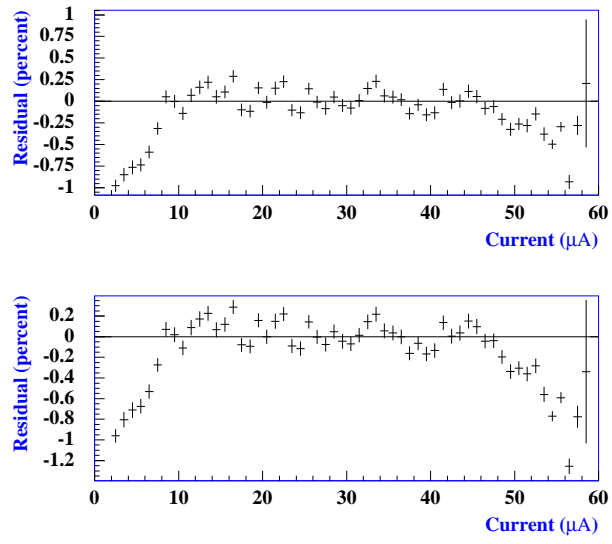


Figure 7: (Color online) (top) Residuals from fit of BCM1 to Unser data, as a fraction of the BCM1 pulse height at 32 μA , versus beam current. (bottom) Same for fit of BCM2 to Unser.

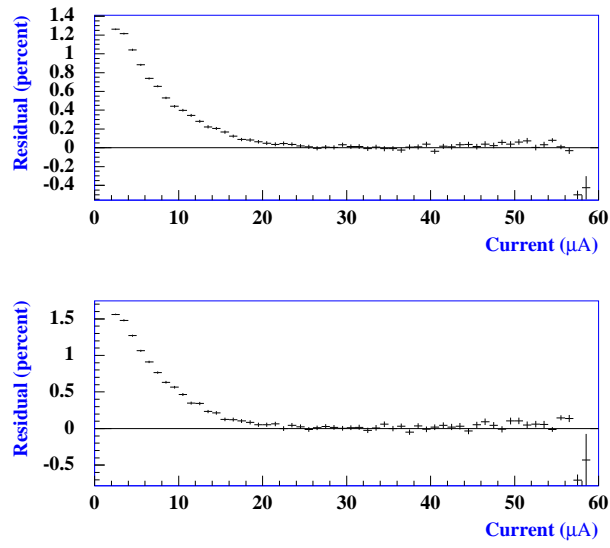


Figure 8: (Color online) (top) Residuals from fit of detector 1 to BCM1 data, as a fraction of the detector 1 pulse height at 32 μA , versus beam current. (bottom) Same for fit of detector 2 to BCM1.

pedestals are negligible.

The cavity monitor pedestals cannot be measured this way, since the cavity signals are meaningless when the beam is off. Instead, we fit $I_{1(2)}$ to I_U in the calibration data and extrapolate to zero current. Such an extrapolation requires knowledge of the average Unser pedestal, which is obtained from the beam-off data in the same run. The resulting pedestals are less than 2% of the signal corresponding to the lowest stable beam current in the production data set.

In conclusion, no corrections for pedestals or nonlinearities needed to be applied. The nonlinearities of the detectors and cavity monitors were negligible over the dynamic range of the beam current we ran. The pedestals for detectors and cavity monitors were negligible.

2.8 Systematic Fluctuations and Beam Corrections

In this section we consider possible corrections from the helicity-correlations in the beam.

If one considers the cumulative corrected asymmetry A_d^{corr} over many window pairs, one can write

$$\begin{aligned}
 A_d^{\text{corr}} &\equiv \langle (A_d^{\text{corr}})_i \rangle = \\
 &\quad \left\langle \left(\frac{\Delta D}{2D} \right)_i \right\rangle - \left\langle \left(\frac{\Delta I}{2I} \right)_i \right\rangle - \sum_j \beta_j \langle (\Delta M_j)_i \rangle \\
 &= A_D - A_I - \sum_j A_{M_j}.
 \end{aligned} \tag{18}$$

For most of the running conditions during data collection, $A_d^{\text{corr}} \simeq A_D \simeq 10$ ppm, which meant that all corrections were negligible. The cumulative average for A_I was maintained below 0.1 ppm. For A_{M_j} , the cumulative averages were found to be below 0.1 ppm during the run. This resulted from the fact that the accelerator damped out position fluctuations produced at the source by a large factor (6).

Adjustments of the circular polarization of the laser beam was required to reduce the differences to about $0.1 \mu\text{m}$. This resulted in observed position differences on target ranging from 10

nm to 100 nm, which in turn resulted in A_{Mj} in the range from 0.1 to 1 ppm. During the run, the control of the asymmetry corrections within the required limits was accomplished with feedback on the laser and electron beam properties in order to maintain small helicity correlations; these methods are discussed in Ref. (6).

The averaged asymmetries and corrections due to the beams are shown in table 2.8.

	Left Kine 1	Left Kine 2	Right Kine 2
A_{raw}	78.43 ± 2.68	140.48 ± 10.43	140.56 ± 6.58
A_{dit}	78.44 ± 2.68	140.29 ± 10.43	140.53 ± 6.58
Correction	0.01 ± 0.10	-0.19 ± 0.25	-0.03 ± 0.03

The uncertainties of the corrections in table 2.8 are estimated by what method ... as shown in table 2.8.

Monitor	Left Kine 1 Correction (ppm)	Left Kine 2 Correction (ppm)	Right Kine 2 Correction (ppm)
4AX	0.025	0.141	0.018
4AY	0.058	0.137	0.001
4BX	0.025	0.131	0.023
4BY	0.066	0.072	0.006
12x	0.002	0.008	0.002
Total	0.095	0.247	0.030

2.9 Background Analysis

numbers awaiting inputs:

- pion and electron asymmetry results from wide triggers;

The above results will affect the pion asymmetry (corrected for electron contamination), which further affect 1) the uncertainty in the main results due to pion contamination, and 2) evaluation of positron results;

- Run-average deadtime correction for unblinding - Diancheng

2.9.1 Charged Pion Background

Charged pions are produced from decays of nucleon resonances created by electron scattering off nucleon or nuclear targets. For the pions to have the same momentum as DIS electrons, the parent nucleon resonance production must occur at a lower Q^2 than DIS events, causing a smaller parity violation asymmetry than DIS electrons. This has been confirmed by the asymmetry of the pion triggers measured during the experiment. Furthermore, the high particle identification performance of the customized DAQ limited the pion contamination in the electron trigger to the $f = 2 \times 10^{-4}$ level or below (9). Due to the small contamination, effect of the pions was considered a dilution and no correction to the measurement electron was made. The total systematic uncertainty on the electron DIS asymmetry due to pion contamination and pion asymmetry is:

$$\Delta A = \sqrt{(\Delta f)^2 + \left(f \frac{|A_\pi| + \Delta A_\pi}{A_e}\right)^2} \quad (19)$$

where f is the event fraction of the electron trigger that is from pions, A_π is the measured pion asymmetry with ΔA_π its uncertainty, and A_e is the measured electron asymmetry. The term $|A_\pi| + \Delta A_\pi$ corresponds to how much the pion asymmetry differs from zero. Results for f and its error bars are presented in Ref. (9). Extraction of the pion asymmetry from the pion trigger asymmetry is described below. The measured electron asymmetries before any corrections is made are 78.4 and 140.5 ppm for $Q^2 = 1.1$ and 1.9 GeV^2 , respectively.

pion asymmetry measurement

PID performance of both electron and pion triggers of the DAQ was reported in Ref. (9). To properly extract pion asymmetries from the trigger, one must properly account for the effect of electron contamination. Because electron contamination in the pion triggers, $f_{e/\pi}$, was relatively high and the electron asymmetries are larger than those of pions, corrections were applied to

Table 1: Pion asymmetry results and total uncertainty on electron asymmetry due to pion background.

HRS Q^2 (GeV/c) ²	Left 1.1	Left 1.9	Right 1.9
narrow path			
raw A_π (ppm)	$-45.79 \pm 7.98(\text{stat.})$	$-14.00 \pm 14.89(\text{stat.})$	$-9.51 \pm 4.22(\text{stat.})$
$f_{e/\pi}$	$0.2738 \pm 0.0563(\text{total})$	$0.0320 \pm 0.0034(\text{total})$	$0.0097 \pm 0.0012(\text{total})$
corrected A_π (ppm)	$-36.86 \pm 10.35(\text{total})$	$-9.95 \pm 15.38(\text{total})$	$-8.24 \pm 4.26(\text{total})$
corrected A_π (ppm)	(tot.)	(tot.)	(tot.)
A_e measured (ppm)	78.4	140.5	140.5
$f_{\pi/e}$	$(1.61 \pm 0.23) \times 10^{-4}$	$(2.20 \pm 0.29) \times 10^{-4}$	$(1.99 \pm 0.24) \times 10^{-4}$
$\frac{\Delta A}{A}$	0.0000925	0.0000490	0.0000296
$\frac{\Delta A}{A}$			
wide path			
raw A_π (ppm)	(stat.)	(stat.)	(stat.)
$f_{e/\pi}$	$0.2246 \pm 0.0541(\text{total})$	$0.02672 \pm 0.00343(\text{total})$	$0.008537 \pm 0.00128(\text{total})$
corrected A_π (ppm)	(tot.)	(tot.)	(tot.)
A_e measured (ppm)	78.4(?)	140.5(?)	140.5(?)
$f_{\pi/e}$	$(1.00 \pm 0.20) \times 10^{-4}$	$(1.83 \pm 0.26) \times 10^{-4}$	$(1.59 \pm 0.22) \times 10^{-4}$
$\frac{\Delta A}{A}$			

the (raw) asymmetries extracted from the pion triggers using

$$A_\pi^{\text{corrected}} = \frac{A_\pi^{\text{raw}} - f_{e/\pi} A_e}{1 - f_{e/\pi}}, \quad (20)$$

where A_e is the electron asymmetry provided from the electron triggers.

electron asymmetry uncertainty due to pion contamination

Results for the pion contamination in electron triggers $f_{\pi/e}$ and the electron contamination in pion triggers $f_{e/\pi}$ and their total uncertainties are shown in Table 1. These results were reported in Ref. (9). Also shown are the raw and the corrected pion asymmetries, and the total uncertainty on the electron asymmetry due to pion contamination as calculated from Eq. 19.

Table 2: Positron asymmetry results.

HRS	Left	Right
Q^2 (GeV/c) ²	1.1	1.9
raw A_{e^+} (ppm), narrow	$723.2 \pm 1154.7(\text{stat.})$	$1216.0 \pm 1304.5(\text{stat.})$
raw A_{e^+} (ppm), wide	$742.4 \pm 1151.5(\text{stat.})$	$1199.0 \pm 1304.5(\text{stat.})$

2.9.2 Pair Production Background

Pair production background comes from nucleon resonance productions where the resonance decays into π^0 's, then through pion decay $\pi^0 \rightarrow e^+e^-$. The pair production from Bremsstrahlung photons is highly forward-peaked and is not significant for the kinematics proposed here. One therefore expect the pair production background to have an asymmetry that is comparable to the charged pion asymmetry reported above. This background was studied during the experiment by reversing the spectrometer polarity, allowing detection of the positron alone in the π^0 decay. The main focus of such positive polarity runs (or “positron runs”) is to precisely determine the fractional contribution from pair production to the main electron trigger, f_{e^+/e^-} . Due to the relative low rate of positron events, this ratio can be extracted from the regular DAQ of which the PID performance and rate determination were well understood. Asymmetry of positrons was recorded, although due to the very low rate of positrons the uncertainty of such asymmetry measurement is large. Results for the asymmetry extracted from positive polarity runs (using the electron triggers of the DAQ, which are now effectively positron triggers) are shown in Table 2. Note that there is a large π^+ contamination in the positron trigger but there was not enough data to correct this π^+ background.

Because the statistical uncertainties of the positron asymmetry results are large, we relied on the fact that π^0 must have similar asymmetry as π^- . We assume the π^0 asymmetry to be no larger than twice the value of π^- asymmetry and estimate the uncertainty in the electron

Table 3: Results for positron contamination f_{e^+/e^-} and total uncertainty on electron asymmetry due to pair production background. The errors shown for f_{e^+/e^-} are statistical only, and a 10% systematic uncertainty was used in the evaluation of $\frac{\Delta A}{A}$.

HRS	Left	Left	Right
$Q^2 \text{ (GeV}/c)^2$	1.1	1.9	1.9
f_{e^+/e^-}	$(2.504 \pm 0.007) \times 10^{-4}$	$(5.154 \pm 0.001) \times 10^{-3}$	$(4.804 \pm 0.001) \times 10^{-3}$
$\frac{\Delta A}{A}$	$2.504 \times 10^{-5} \circ + ???$	$5.154 \times 10^{-4} \circ + ???$	$4.804 \times 10^{-4} \circ + ???$

asymmetry due to positron background as:

$$\Delta A = \sqrt{\left(\Delta f_{e^+/e^-}\right)^2 + \left(f_{e^+/e^-} \frac{\Delta A_{e^+}}{A_e}\right)^2}, \quad (21)$$

where ΔA_{e^+} describes how much A_{e^+} differs from zero and the value $2(|A_\pi| + \Delta A_\pi)$ was used. Results for f_{e^+/e^-} and their statistical errors are shown in Table 3, and a 10% systematic uncertainty is used for $\Delta f_{e^+/e^-}$ to account for possible error in positron identification from the high π^+ background in the rate evaluation. Results for the electron asymmetry uncertainty due to pair production background are also shown in Table 3.

2.9.3 Target EndCap Correction

Electrons scattered off the target aluminum endcaps cannot be separated from those scattered off the liquid deuterium. Fortunately events from target endcaps also belong to deep inelastic scattering and one expect the DIS formula for asymmetries (refer to equation in “formalism”) to work for aluminum as well. Since Al is not an isoscalar nucleus, the Al PVDIS asymmetry differs from the deuterium and a correction must be made. Possible deviations for A_{Al} to differ from the DIS formula is the nuclear effect similar to the EMC effect of the unpolarized, parity-conserving structure functions $F_{1,2}$, but one does not expect such effect to cause more then 20% difference to A_{Al} and this assumption will be used in the uncertainty estimation.

The fractional event rate from the aluminum endcaps, $f_{Al/D}$, is assumed to be equal to the ratio of the endcap to liquid deuterium thickness, $\eta_{Al/D}$. This is based on the assumption that the

DIS cross section from Al is the same as that from D₂. Using current data on the EMC effect, the difference in DIS cross sections between Al and LD₂ indeed should be very small since the EMC ratio crosses unity between $x = 0.2$ and 0.3 , exactly where data were taken during this experiment. The target used for this experiment had entrance and exit endcaps measured to be $0.126 \pm 0.011 \pm 0.003$ mm and $0.100 \pm 0.008 \pm 0.003$ mm respectively, with the first error bar from the standard deviation of multiple measurements at difference positions on the endcap, and the second error from calibration of the instrument. The ratio $\eta_{Al/D}$ is evaluated to be $\eta_{Al/D} = (0.126 + 0.100) \text{ mm} \times 2.7 \text{ g/cm}^3 / (20 \text{ cm} \times 0.167 \text{ g/cm}^3) = 1.827\%$ with a total error of 0.115%.

The correction to the electron PVDIS asymmetry is applied as

$$A^{corrected} = A^{measured}(1 + \delta_{Al}), \text{ with } \delta_{Al} = -(\eta_{Al/D}) \frac{A_{Al} - A_D}{A_D}. \quad (22)$$

The DIS formalism was used to evaluate the Al PVDIS asymmetry as:

$$A_{Al} = \frac{13A_p\sigma_p + 14A_n\sigma_n}{13\sigma_p + 14\sigma_n}, \quad (23)$$

where $\sigma_{p(n)}$ is the DIS cross section off the proton (neutron) as calculated from structure function fits and $A_{p(n)}$ is the PVDIS asymmetry off the proton (neutron):

$$A_p = \left(-\frac{3G_F Q^2}{2\sqrt{2}\pi\alpha} \right) \frac{Y_1 [2C_{1u}(u^+ + c^+) - C_{1d}(d^+ + s^+)] + Y_3 [2C_{2u}(u^-) - C_{2d}(d^-)]}{4(u^+ + c^+) + (d^+ + s^+)} \quad (24)$$

$$A_n = \left(-\frac{3G_F Q^2}{2\sqrt{2}\pi\alpha} \right) \frac{Y_1 [2C_{1u}(d^+ + c^+) - C_{1d}(u^+ + s^+)] + Y_3 [2C_{2u}(u^-) - C_{2d}(d^-)]}{4(d^+ + c^+) + (u^+ + s^+)} \quad (25)$$

with $u^\pm \equiv u \pm \bar{u}$, $d^\pm \equiv d \pm \bar{d}$, $s^+ \equiv s + \bar{s}$ and $c^+ \equiv c + \bar{c}$.

The total uncertainty due to target endcaps, assuming an up to 10% difference in the Al vs. D₂ PVDIS asymmetry, is approximately

$$\frac{\Delta A}{A} = \sqrt{(\Delta\eta_{Al/D})^2 + ((10\%) \eta_{Al/D})^2} \quad (26)$$

Table 4: Correction applied to the measured asymmetry to account for the target aluminum endcaps.

$Q^2 \text{ (GeV/c)}^2$	1.1	1.9
$(A_{Al} - A_D)/A_D$	0.005670	0.007268
δ_{Al}	-1.036×10^{-4}	-1.328×10^{-4}
$\frac{\Delta A}{A}$	0.001827	0.001827

where the second term dominates. Results for the endcap correction δ_{Al} and the uncertainty on the corrected electron asymmetry are given in Table 4.

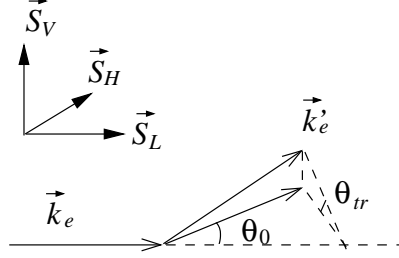
Events were also taken on a thick, “dummy” target consists of two thick aluminum endcaps the thickness approximately 10 times that of the liquid deuterium cell. The thickness was chosen such that the total radiation length of the dummy target matches that of the liquid D₂ target. However, due to limited beam time, the asymmetry uncertainty collected from the aluminum dummy target was not precise enough to reduce the systematic uncertainty due to target endcaps.

2.9.4 Transverse Asymmetry Background

Transverse asymmetry background describes the effect of the electron beam spin polarized in the direction perpendicular (normal) to the scattering plane defined by the momentum vectors of the incident and the scattered electrons \vec{k}_e and \vec{k}'_e . This beam normal asymmetry is parity violating but differs from the PVDIS asymmetry caused by the longitudinal polarization of the beam, thus must be treated as a background of the measurement. Calculations at the pure partonic level show that this asymmetry is at the 0.5 ppm level at the kinematics of this experiment, but mechanism beyond the parton level can enhance the asymmetry by 1-2 orders of magnitude (26 latest email 10/29/2012). Contribution from the beam normal asymmetry A_n to the measured asymmetry can be expressed as

$$\delta A = (A_n) \vec{S} \cdot \hat{k}_n \quad \text{with} \quad \vec{k}_n \equiv \hat{k}_e \times \hat{k}'_e \quad \text{and} \quad \hat{k}_n = \vec{k}_n / |\vec{k}_n|, \quad (27)$$

Figure 9: Kinematics of the transverse asymmetry background. The incident and the scattered electrons' momenta are \vec{k}_e and \vec{k}'_e , and $\vec{S}_{V,H,L}$ denote respectively the incident electron's spin polarization components in the vertical, horizontal, and longitudinal directions. The central scattering angle of the spectrometer is θ_0 and the scattered electron's momentum has an out-of-plane angle denoted by θ_{tr} .



where \vec{S} is the beam polarization vector. Denoting θ_0 the central scattering angle of the spectrometer and θ_{tr} the average out-of-scattering-plane angle of the spectrometer acceptance as defined in Fig. 9, one has $\hat{k}_e = (0, 0, 1)$ and $\hat{k}'_e = (\sin \theta_0 \cos \theta_{tr}, \sin \theta_0 \sin \theta_{tr}, \cos \theta_0)$, giving $\vec{k}_n = (-\sin \theta_0 \sin \theta_{tr}, \sin \theta_0 \cos \theta_{tr}, 0)$ and $\hat{k}_n = (-\sin \theta_{tr}, \cos \theta_{tr}, 0)$, thus

$$\delta A = A_n [-S_H \sin \theta_{tr} + S_V \cos \theta_{tr}] \quad (28)$$

where S_V , S_H and S_L are respectively the electron's spin polarization components in the vertical, horizontal, and longitudinal directions. The value of θ_{tr} was determined from the simulation and was found to be less than 0.01 rad. Since the beam spin during production runs was controlled to $S_H < 20\%P_b$ and $S_V < 2\%P_b$ where P_b is the beam polarization, the S_V term dominates the effect on the measured asymmetry.

During the experiment, the size of the beam transverse asymmetry was measured during dedicated “transverse runs” where the beam was fully polarized in the vertical direction, $S_H = S_L \approx 0$ and $S_V = P_b^T$ where P_b^T is the beam polarization during the transverse asymmetry measurement. The measurement thus provides the value $A_n^m = A_n P_b^T$. Since the maximum beam polarization is the same for production and transverse asymmetry running, and the hor-

Table 5: Results from the dedicated beam transverse asymmetry measurements and estimation of the total uncertainty on the PVDIS electron asymmetry due to beam transverse polarization.

HRS Q^2 (GeV/c) ²	Left 1.1	Right 1.9
A_n^m (ppm, narrow)	-24.15 ± 15.05	23.49 ± 44.91
A_n^m (ppm, wide)	-24.66 ± 15.01	24.60 ± 44.90
A_e^m (ppm)	78.4	-140.5
$\frac{\Delta A}{A}$	0.014195	0.00717

horizontal component of the beam spin S_H is no more than 20% during the production runs, the longitudinal beam polarization during production running, S_L , cannot differ from P_b^T by more than $1 - \sqrt{1 - (20\%)^2} = 1.01\%$. The total uncertainty in the PVDIS electron asymmetry can be estimated using

$$\frac{\Delta A}{A} = \frac{(|A_n^m| + \Delta A_n^m)}{A_e^m} \sqrt{[S_V^2 + (1.01\%)^2]} = 0.0224 \frac{\delta A_n^m}{A_e^m} \quad (29)$$

where δA_n^m describes how much A_n could differ from zero and is taken to be ΔA_n^m if the measured asymmetry is consistent with zero and $(|A_n^m| + \Delta A_n^m)$ otherwise; A_e^m is the measured PVDIS electron asymmetry.

Results for the beam transverse asymmetry measurements are shown in Table 5 along with the total uncertainty on the electron PVDIS asymmetry results due to beam transverse polarizations.

Total error previously quoted: 0.34%, 0.56% (a factor of $\sin \theta_0$ was used which suppressed the effect).

2.9.5 Target Purity, Density Fluctuation and Other False Asymmetries

the following is copied from the proposal and must be revised.

The liquid deuterium used contains (27) 1889 ppm HD, < 100 ppm H₂, 4.4 ppm N₂, 0.7 ppm O₂, 1.5 ppm CO, < 1 ppm methane and 0.9 ppm CO₂. Since most of these are isoscalar nuclei, the only non-negligible effect on the measured asymmetry comes from the proton in HD. The proton asymmetry is given by Eq. 24 which is within $\pm 10\%$ (??? check) of the asymmetry of the deuteron, the proton in HD therefore contribute an uncertainty of less than $\Delta A/A < 0.02\%$ uncertainty to the measured asymmetry.

2.10 Rescattering Background

the following is copied from the proposal and must be revised.

The rescattering of high-energy electrons or pions from the walls of the spectrometer creates a potential source of background for the proposed measurement. This “rescattering” background, which is typically rejected using a combination of tracking and particle identification in low-rate experiments without difficulty, must be treated carefully in this high-rate measurement due to the limited information available in each event.

The magnitude of this effect will be combination of the probability for products of this scattering in the spectrometer to reach the detectors and how far their kinematics (Q^2, x) differ from the PVDIS events.

Rescattering probability has been studied by the previous HAPPEX II experiments in Hall A (HAPPEX-H: E99-115 and HAPPEX-He: E00-114) (6). The method used includes a series of dedicated elastic scattering measurements with a hydrogen target, with the spectrometer tuned to place the hydrogen elastic peak at various points inside the spectrometer. The detected rate was used to estimate the “rescattering probability”: the probability that an electron, interacting at a given point in the spectrometer, produces a count in the production DAQ. In those measurements, the rescattering probability was found to be around 1% for momenta near to the central

momenta (within a few percent of $\delta p/p$). This probability rapidly dropped to 10^{-5} for interactions with the spectrometer wall took place before the last spectrometer quadrupole element (Q3).

Using the nominal momentum acceptance of the spectrometer, $\pm 4.5\%$, the rescattering background just outside this range would have a Q^2 about $(4.5 - 5)\%$ different from DIS events that entered center of the spectrometer.

It is reasonable to expect that the detected rescattering signal in the proposed measurement will also form a dilution at the few 10^{-3} level. Factors that would argue for a larger contribution, such as the continuous DIS momentum distribution and the relatively open spectrometer geometry, will be counteracted by the ability to exclude background through position, energy, or PID information from the fast counting DAQ.

Overall, we expect that the total rescattering rate to be at most at a few $\times 10^{-3}$ level. And among these rescattered events, resonance electrons and pions will only consist a small fraction. The rescattered DIS electrons may be the majority of these rescattering events but they have very similar kinematics and Q^2 to the primary measurement thus will only introduce a very small dilution. Therefore we expect the total uncertainty due to the rescattered background to be in the 10^{-4} range.

2.11 Calibration of the HRS Optics

In this section the procedure for calibrating the scattering momentum, angle, and event position is described in details. An overview of the Hall A coordinate systems is presented first. Note that that a reference to an angular coordinate in this section should always be taken as the tangent of the corresponding angle.

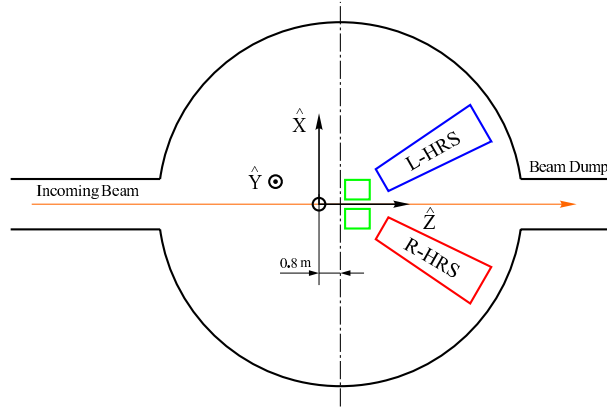


Figure 10: Hall coordinate system (top view)

2.11.1 Hall Coordinate system (HCS)

The origin of the HCS is defined by the intersection of the electron beam and the vertical symmetry axis of the target system. Direction \hat{z} is along the beam line and points to the beam dump, \hat{y} is vertically up and \hat{x} is to the right facing the beam (See Figure10).

2.11.2 Target Coordinate System (TCS)

Each of the HRS is bundled with its own TCS. The central ray vertically passing through the center of sieve collimator away from target defines the z_{tg} axis of the TCS for a given spectrometer. The \hat{y}_{tg} is pointing to the right and \hat{x}_{tg} is vertically down facing the central ray. In the ideal case where the spectrometer is pointing directly at the hall center and the sieve slit is perfectly centered on the spectrometer, the TCS has the same origin as HCS. However it typically deviates from HCS center by D_y and D_x in horizontal and vertical directions in TCS. And these shifts are given by survey. The distance of midpoint of the collimator from the TCS origin is defined to be a constant L for the spectrometer. The out-of-plane angle (θ_{tg}) and the in-plane angle (ϕ_{tg}) are given by dx_{sieve}/L and dy_{sieve}/L (See Fig. 11).

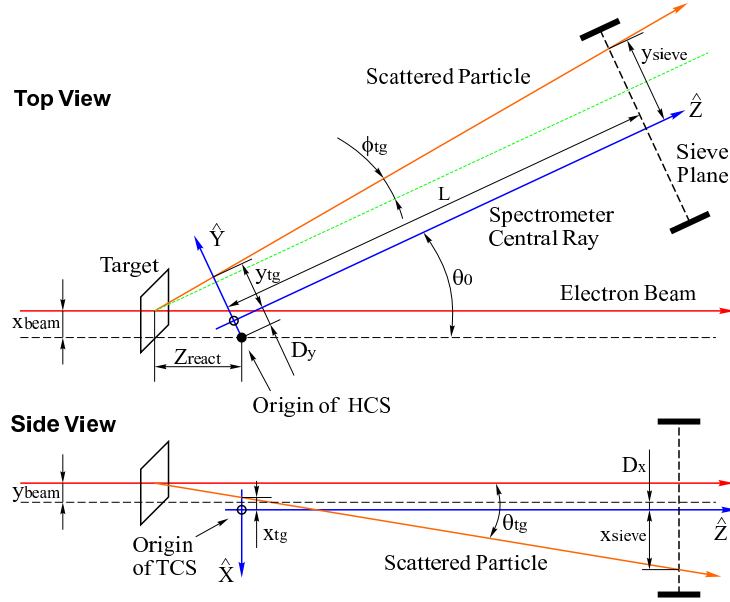


Figure 11: Target coordinate system (top and side views).

2.11.3 Detector Coordinate System (DCS)

The interaction of wire 184 of the VDC1 U1 plane and the perpendicular projection of wire 184 in the VDC V1 plane onto the VDC U1 plane defines the origin of the DCS. \hat{z} is perpendicular to the VDC planes pointing vertically up, \hat{x} is along the long symmetry axis of lower VDC pointing away from the hall center (See Fig. 12).

2.11.4 Transport coordinate System (TRCS)

The TRCS at the focal plane is generated by rotating the DCS clockwise around its y -axis by 45 degrees. It's typically used as a mediate stage from DCS to the FCS which will be described in next section. Ideally, the \hat{z} of the TRCS coincides with the central ray of the spectrometer (See Fig. 13).

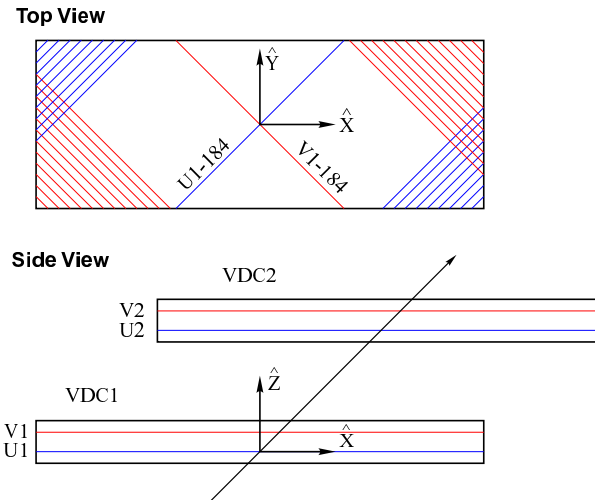


Figure 12: Detector coordinate system (top and side views).

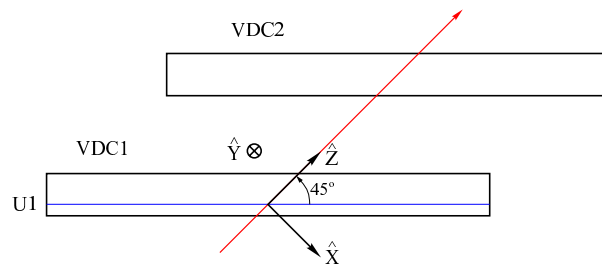


Figure 13: Transport coordinate system.

2.11.5 VCD Timing Calibration

The typical drift time spectrum of a wire plane is shown in the Fig. 14 where the drift times of all the wires in a plane are plotted in terms of TDC channels.

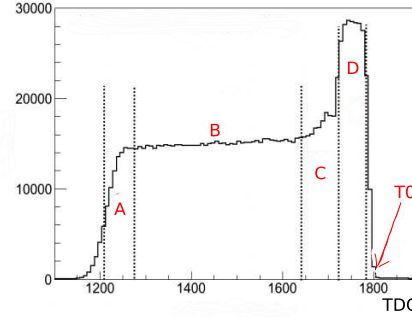


Figure 14: A drift-time Spectrum of a VDC plane.

The TDCs were operated in common-stop mode and hence the large TDC values correspond to the short drift times. The various regions in the spectrum can be understood as follows:

- **Region A:** This is a region that corresponds to the particles having larger trajectory angles and hence are further away from the drift cell around the sense wires.
- **Region B:** This region has all the field lines parallel and hence the drift velocity of the electrons is constant.
- **Region C:** In this region, the field lines begin to change from parallel to quasi-radial closer to the sense wires and as a result, the probability of detecting a particle begins to increase.
- **Region D:** This region corresponds to a region very close to the sense wires where the drift velocity of the electrons increases drastically and probability of detecting a particle is maximal. In order to compare and use the drift time spectra from all the wires in a

plane, a reference timing T_0 for all the wires had to be defined so that the various timing offsets due to variable cable lengths and signal processing times for different wires could be eliminated. The calibration procedure, thus, involved the determination of T_0 for each wire in the plane and matching each of them to one common reference point. T_0 for each wire was determined by differentiating the region of short drift times around channel 1800 numerically and looking for the maximum slope. Once the maximum slope was calculated, it was extrapolated to the channel axis and the point of intersection of the extrapolation and the axis was determined as shown in Fig.14. Each of the four planes in the two VDCs was calibrated and the reference T_0 was determined. This corresponds to 0 ns in the corrected timing spectrum. Figure 15 shows the drift-time spectrum of the VDC U1 plane before and after T_0 timing calibration.

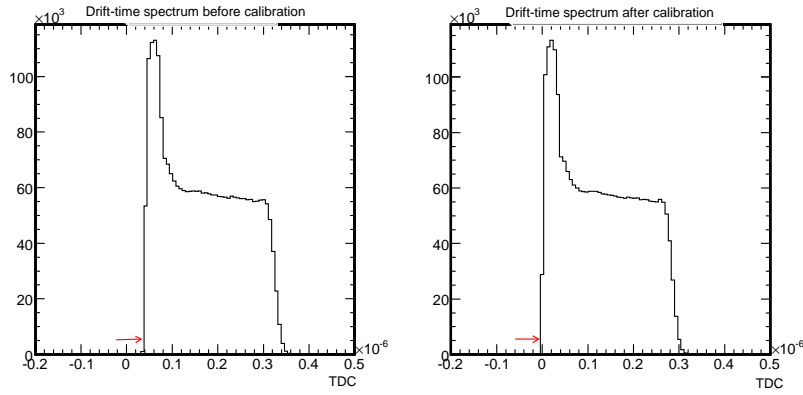


Figure 15: Drift-time spectrum of VDC U1 plane before (left) and after (right) T_0 timing calibration.

2.11.6 Beam Position Calibration

The beam position is reconstructed through a linear transformation of the raster current using offsets and scaling coefficients obtained from the BPMs' position distributions and the raster's

current distribution. There are two BPMs upstream of the target used to determine the beam's position. When using a rastered beam, however, the BPMs are too slow to measure the event-by-event position. The current in the raster magnets can be used directly to calculate the beam deflection and beam position. Using the raster current to determine the beam position requires beam position calibration from raster current. The procedure for the calibration is as following:

1. Calculate the raster current to beam position transformation coefficients. The relation between the current in the raster and the beam deflection/position depends on beam energy and beam tuning. Therefore the raster current to beam position calibration must be checked for all data. The transformation coefficients are found using the script `get_raster_coeff.C`. The script works as follows:

- Get the mean and rms values of the distribution of the rastered beam's position using the BPMs (e.g. `urb.BPMA.x`)
- Get the mean and rms values of the distribution of the current in the raster (e.g. `rb.Raster.rawcur.x`)
- Perform calculations to obtain scaling and offset coefficients. Calculations are of the form:

$$\text{bpm offset } x = \langle \text{bpm } x \rangle + \langle \text{raster current } x \rangle \times \frac{\sigma_{bpm,x}}{\sigma_{\text{raster current}}} \quad (30)$$

2. Create new beam `db.dat` files for each run as needed with raster block adjusted accordingly.

3. Replay the coda run again and check the calibration. One can perform the check using the script `calib.C`. This script plots the beam position as determined by the BPMs with the beam position as determined by the raster current. If properly calibrated, they should both have the same mean and RMS values.

4. Fig.16 and Fig.17 shows the results of beam position reconstruction before and after

BPM calibration respectively. The blue line is the beam position as determined by the BPMs, and the red line is the beam position as determined by the raster current.

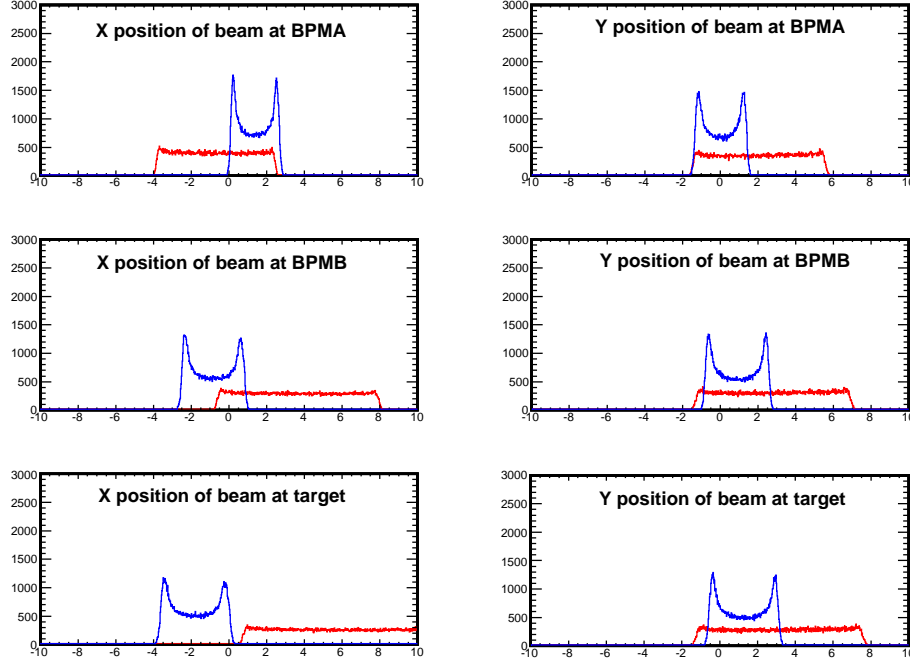


Figure 16: Beam position reconstruction before BPM calibration. The blue line is the beam position determined by the BPMs, and the red line is the beam position determined by the raster current.

2.11.7 General Approach

The optics of the HRS describes the transportation of charged particle from the target side to tracking detector, vertical drift chamber and the optics reconstruction describes the inverted optics transportation property of the magnet, i.e., using the tracking information at the detector side and beam location to reconstruct the momentum and vertex of the scattered particle at the target side. The optics reconstruction for the Left HRS is parameterized using a set of polynomial expansions. The polynomial coefficients are also known as the optics matrix. The

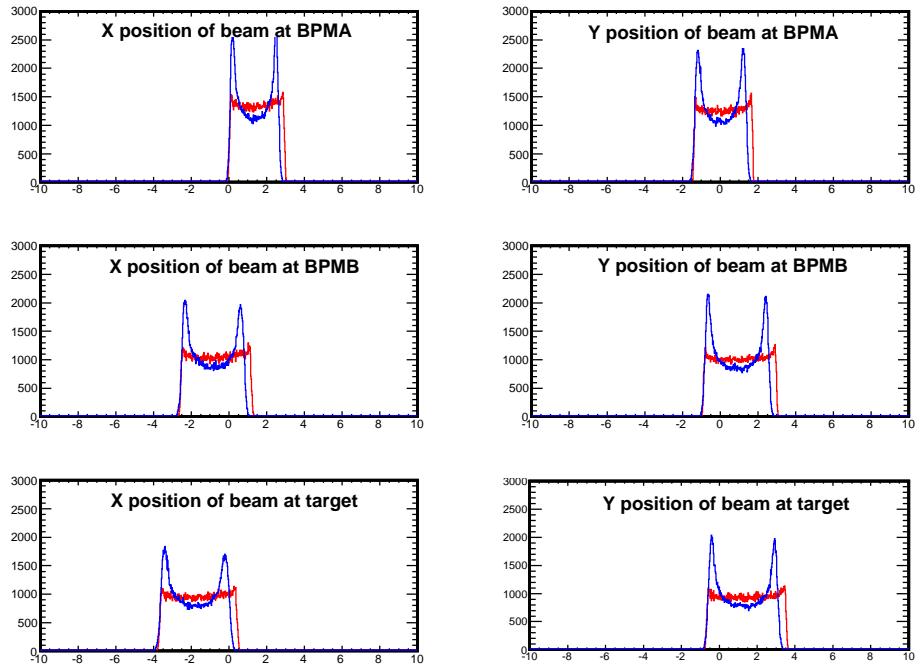


Figure 17: Beam position reconstruction after BPM calibration. The blue line is the beam position determined by the BPMs, and the red line is the beam position determined by the raster current.

optics calibration for PVDIS will be discussed in this section, and result will be presented in next section.

The goal of this study is to calibrate the reconstruction of the following HRS optics variables, which describes the particle trajectory at the target interaction point:

- θ_{tg} and ϕ_{tg} , the tangent of the vertical and horizontal angles relative to the HRS central line.
- Y_{tg} and Z_{react} , are the horizontal track position in the target coordinate system and the vertex position along the ideal beam direction, respectively. They are directly related geometrically as in Fig. 11.

A new optimization routine was established for general HRS optics calibrations. This new code features:

- To ensure the code reproduce exact the same optics reconstruction as the analyzer, the subroutine is converted from the optics reconstruction subroutine THaVDC in the standard ANALYZER. This subroutine is called for thousands of times during the optimization and the coefficients for the optics reconstruction (i.e., optics matrix) are gradually adjusted to minimize the square error defined in Eq.31.
- Minimization routine is based on the MINUIT2 numerical software package.
- Automatically visualize results after optimization.
- Multiple self-consistency checks, including checks on the array size limits, on the input file formats and on the internal results.

2.11.8 Calibration Procedure

The optics calibration requires data sets for which the optics variables are known at both the vertex and detector locations. The optics matrix was obtained by minimizing

$$\chi^2 = \sum (\text{reconstructed target variable} - \text{nominal target variable from survey})^2 \quad (31)$$

Two calibration data sets were taken during the experiment. Each of them provided a calibration for one or two of the target variables. Each target variable was fitted independently.

1. **Vertex calibration** used DIS scattering data on the multi-carbon foil target. All reconstructed foil vertex peaks were aligned to their actual positions as shown in Fig. 18.
2. **The Angular calibration:** Each optics event corresponded to a specific carbon foil and one of the holes in the sieve slit, whose location was surveyed during the experiment. Therefore the actual angle of the vertex trajectory was known for each event. The vertical (θ_{tg}) and horizontal (ϕ_{tg}) tangent angles were independently fit. The final reconstructed sieve-slit plate is shown in Fig. 18 for Left-arm DIS#1 kinematics configuration. Two of the sieve holes are larger than the rest to allow identifying the center and orientation of the sieve, and the corresponding reconstructed larger holes in Fig. 18 have more statistics than the surrounding holes. The sieve-slip plate is larger than the acceptance of the HRS so that the full acceptance can be calibrated. At the edge foils (e.g., the most upstream foils #0 and downstream foil#5), the HRS acceptance is very limited for DIS#2 kinematics configuration as shown in Figs. 20 and 21.

2.11.9 Optics Runlist Summary

In PVDIS experiment, there are seven kinematics settings in total, namely DIS#1, Left-arm DIS#2, Right-arm DIS#2, Res#3, Res#4, Res#5 and Res#7. We conducted optics calibration

runs on each of these seven kinematics settings. Table 6 listed all the optics calibration runs with corresponding run information.

2.11.10 Result

The vertex and angle calibration results for all seven kinematic settings are shown as following. Detailed discussion about the reconstruction uncertainty is discussed in next section.

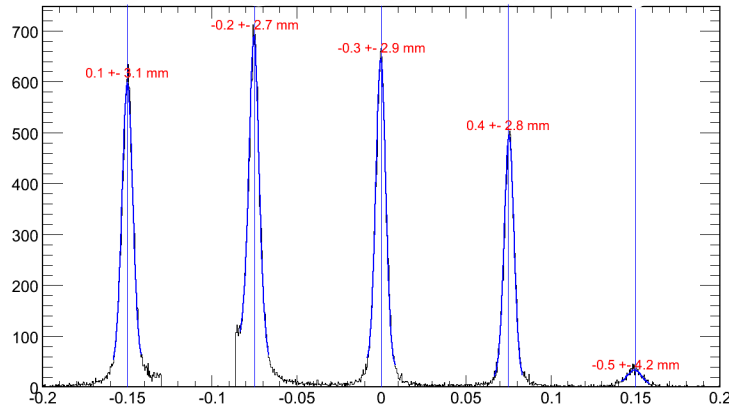


Figure 18: Vertex reconstruction of left kinematics 1.

2.11.11 Q^2 Uncertainties

Optics calibration contributes to Q^2 uncertainties in the following ways:

- $\delta(= dp/p)$ affect E' directly. With calibrations such as water target at one-pass, it can reach $\pm 1 \times 10^{-4}$ level of accuracy. Due to HRS dipoles are very stable and highly reproducible, it is safe to quote $\pm 5 \times 10^{-4}$ as accuracy if there is no calibration carried out.

Date	Description	Run#(L/R)	Raster	Sieve	Magnet (GeV)	Angle (°) (L/R)	Beam Energy (GeV)
11/07/09	survey available	25303/4832	on	out	3.66(L)/ 2.63(R)	12.9(L)/ 20(R)	6.067
	DIS 1,2	25304/4833	off	out			
		25311/4856	on	out			
		25333/4858	off	out			
		25334/4859	off	out			
		25605/5159	on	out			
12/10/09	survery available	26128/5640	off	out	2.63(L)/ 2.63(R)	20(L)/ 20(R)	6.067
	DIS2	26129/5641	on	out			
		26130/5642	off	out			
		26131/5643	on	out			
12/18/09	Res 3(L) Res5(R)	26332/5836	off	out	4/3.66/ 4/3.66(L)/ 3.1(R)	12.9(L)/ 12.9(R)	4.8673
	Magnet Mistuned	26333/4837	on	out			
		26334/5838	on	in			
		26335/5839	off	in			
12/19/09	Res 3(L) Res 5(R)	26386/5876	off	out	3.66(L)/ 3.1(R)	12.9(L)/ 12.9(R)	4.8673
		26387/5877	on	out			
		26389/5878	on	in			
		26390/5879	off	in			
	Res 7(L)	26395/5884	on	out	3.66/3.349/ 3.66/3.349(L)/ 3.1(R)	12.9(L)/ 12.9(R)	4.8673
	Magnet Mistuned	26396/5885	off	out			
		26397/5886	off	in			
		26398/5887	on	in			
	Res 4(L), Res 5(R)	26402/5891	off	out	3.55(L)/ 3.1(R)	12.9(L)/ 12.9(R)	4.8673
		26408/5897	on	out			
		26409/5898	on	in			
		26410/5899	off	in			

Table 6: Optics Run Summary

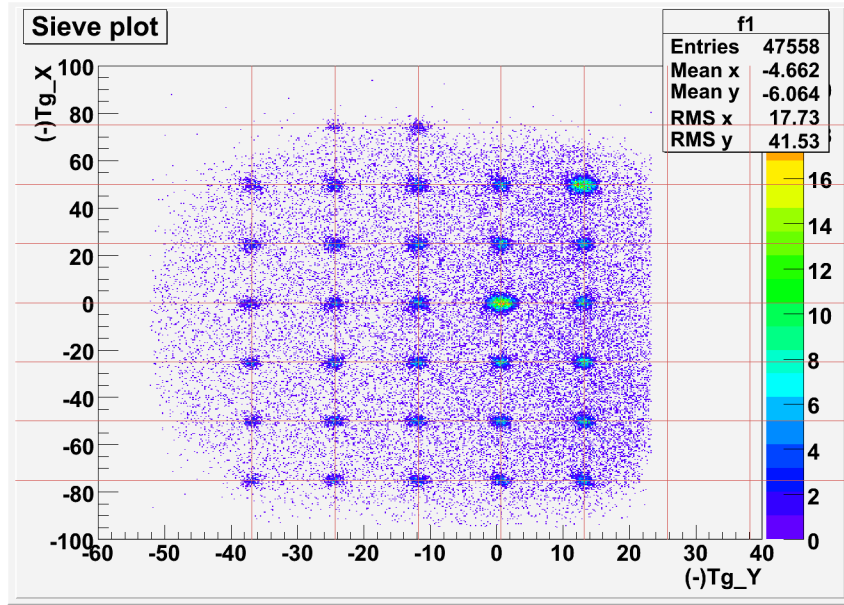


Figure 19: Sieve reconstruction of left kinematics 1.

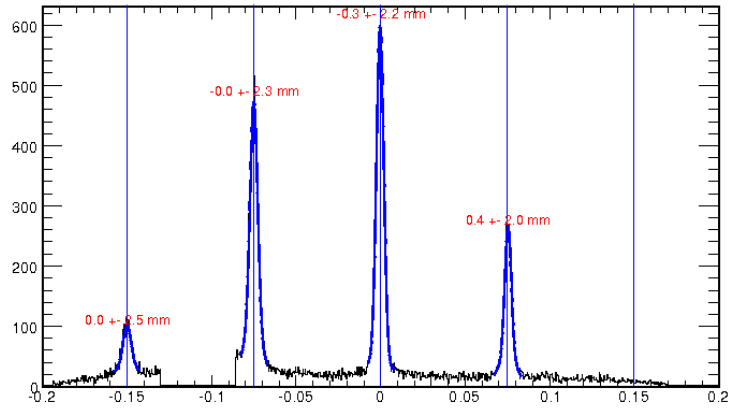


Figure 20: Vertex reconstruction of left kinematics 2.

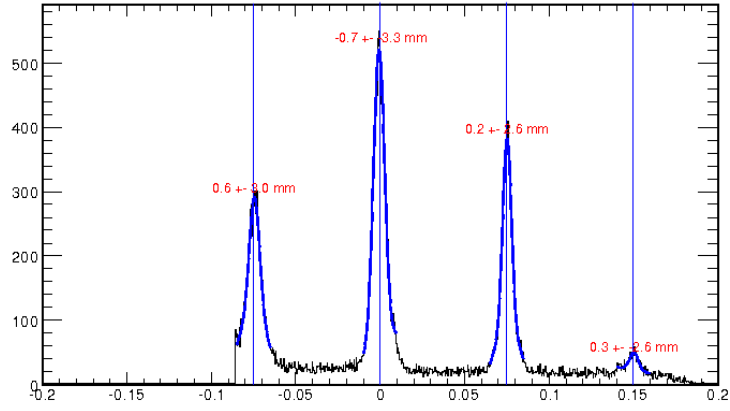


Figure 21: Vertex reconstruction of right kinematics 2.

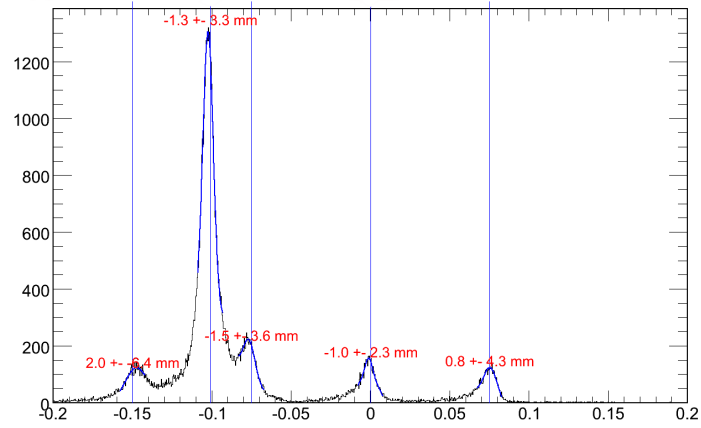


Figure 22: Vertex reconstruction of resonance kinematics 3.

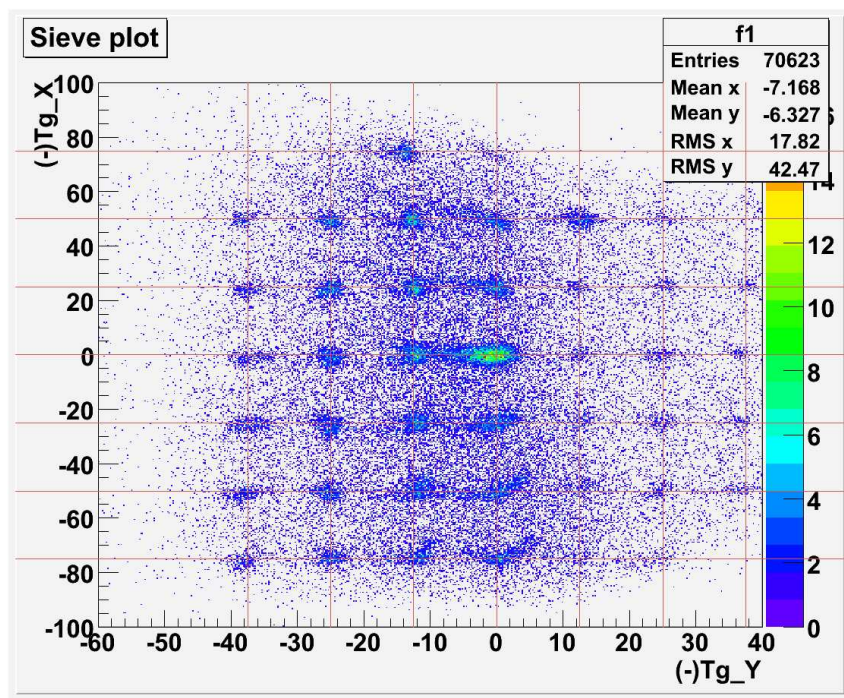


Figure 23: Sieve reconstruction of resonance kinematics 3.

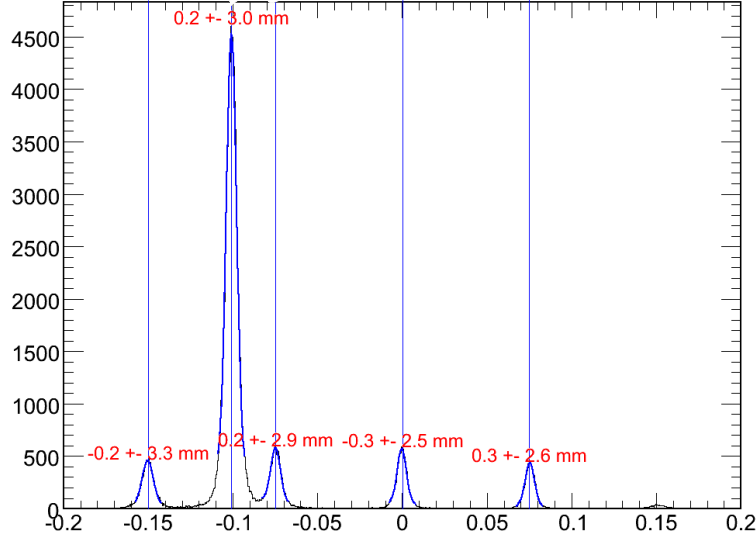


Figure 24: Vertex reconstruction of resonance kinematics 4.

- vertex (Y_{tg}) optimization affect scattering angle. We make the following asumptions to estimate Q^2 uncertainties due to vertex optimization.
1. Pointing offset “D” with survey: error is $\pm 0.5mm$.
 2. “D” derived from data (such as for PVDIS 2nd 12.9 degree setting of LHRS): if a good Y_{tg} optimization is done and the only thing changed is spectrometer pointing, which can be clearly derived from data, the error would be $\pm 0.5mm$, i.e. the same as that from survey.
 3. target position: The uncertainty of target position is expected to be within a few mm of zero in reactZ. Typical quoted uncertainty is $\pm 2.5mm$.
 4. “Goodness” of Y_{tg} optimization: we use the biggest discrepancy between reconstructed

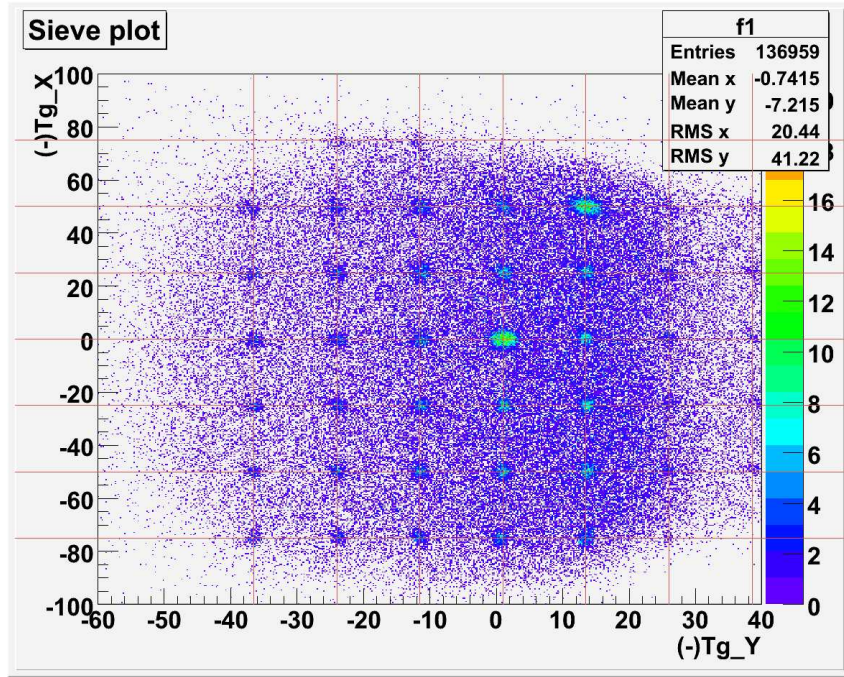


Figure 25: Sieve reconstruction of resonance kinematics 4.

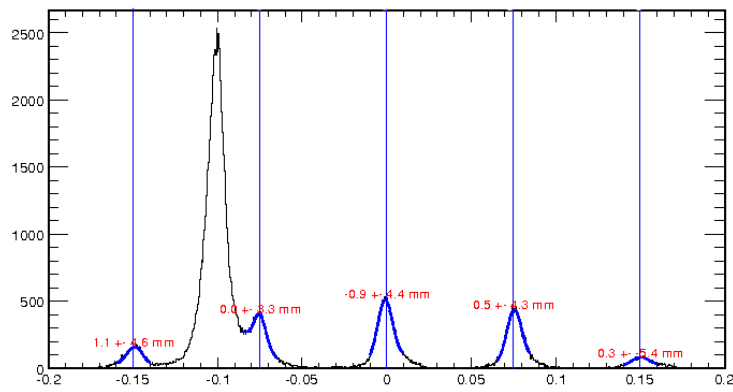


Figure 26: Vertex reconstruction of resonance kinematics 5.

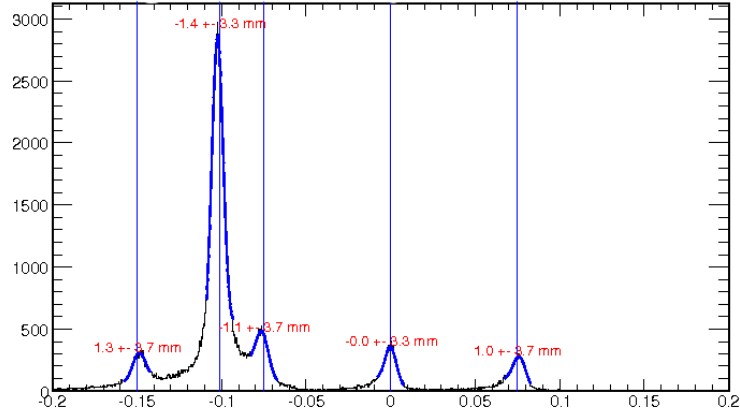


Figure 27: Vertex reconstruction of resonance kinematics 7.

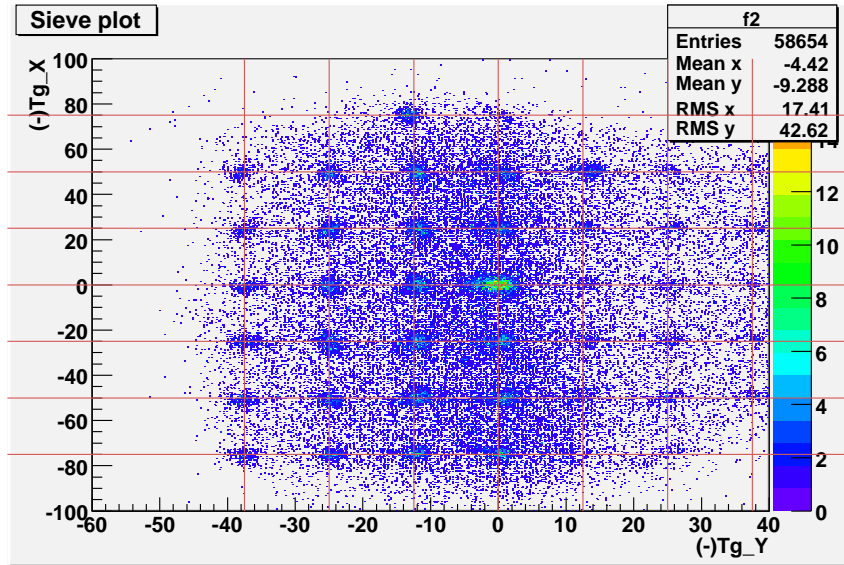


Figure 28: Sieve reconstruction of resonance kinematics 7.

positions and expected position among all five carbon foils peaks as the upper limit of its uncertainty on Y_{tg} optimization.

5. The total uncertainty on the scattering angle is the uncertainty of “D” and that of target position contributed in Y_{tg} added in quadrature, then divided by 1.12m (drift distance between the target center and the HRS entrance).
- angle (θ_{tg} and ϕ_{tg}) optimization directly affect scattering angle. The following assumptions about uncertainty estimation are made.
1. uncertainties on offsets from survey are $\pm 0.5mm$ for both horizontal and vertical.
 2. If there were no work done on the sieve plate (such as taking it off and putting it back on Q1), the vertical position is reproducible to $\pm 0.5mm$. The horizontal position is reproducible to $\pm 0.1mm$.
 3. Discrepancy between observed hole positions and the expected positions is set as $\pm 0.1mm$, if no obvious difference is seen after good angle calibrations.
 4. The total uncertainty on the scattering angle is the uncertainty of sieve hole position divide by 1.12m (drift distance between the target center and the HRS entrance).
 5. In right HRS run, there is no sieve slit data available. Hence, we use HAPPEX optics database. An additional $\pm 0.5mrad$ uncertainty is added on uncertainty. This is the change that we see on left arm angle calibration between using HAPPEX database and PVDIS database.

With above assumptions, we can calculate the Q^2 uncertainties due to the current optimized optics database, which forms the table below for all kinematics settings.

	LHRS					RHRS	
Kinematics	DIS#1	DIS#2	Res#3	Res#4	Res#7	DIS#2	Res#5
Angle θ	12.9	20	12.9	12.9	12.9	20	12.9
E'	3.66	2.63	4.0/3.66/4.0/3.66	3.66	3.66/3.349.3.66/3.349	2.63	3.1
HRS angle survey	Y	Y	N	N	N	Y	N
Carbon multi foil data	Y	Y	Y	Y	Y	Y	Y
D (from survey)(mm)	0.5	0.5				0.5	
D(from data)(mm)			0.5	0.5	0.5		0.5
reactZ from ytarg optimization(mm)	0.3	0.4	2	0.3	1.4	0.7	1.1
reactZ from target position(mm)	2.5	2.5	2.5	2.5	2.5	2.5	2.5
$\sin(\theta)$ term, to be used for reactZ	0.22	0.34	0.22	0.22	0.22	0.34	0.22
sieve survey	N	N	N	N	N	N	N
sieve data			Y	Y	Y		
sieve horizontal position, absolute (mm)	0.51	0.51	0.51	0.51	0.51	0.51	0.51
sieve horizontal position, calibration results (mm)	0.1	0.1	0.1	0.1	0.1	0.1	0.1
horizontal angle using HAPPEX database(mrad)						0.5	0.5
Total angle uncertainty(mrad), using 1.12m d.d	0.812	1.003	0.900	0.812	0.855	1.134	0.976
Total angle uncertainty, relative(%)	0.361	0.287	0.400	0.361	0.380	0.325	0.434
Total Q2 uncertainty(%)	0.722	0.575	0.800	0.722	0.760	0.650	0.868

Table 7: PVDIS Q² Uncertainty

2.12 Reconstruction of Q^2 and x (HAMC)

The four-momentum transfer squared is

$$Q^2 = 2 E E' (1 - \cos(\theta)) \quad (32)$$

where E is the incident energy, E' is the final momentum or energy of the electron ($E' \gg m_e$) and θ is the scattering angle.

For the beam energy we used the Tiefenbach energy (need to explain this) of ??? GeV and assumed a 3 MeV (???) average energy loss to the center of the target which is applied this as a correction to the beam energy. The error in the beam energy E and E' are assumed conservatively to be 3 MeV based on a history of these measurements in Hall A. The most important error is in θ ...

Perhaps need a table of errors.

A simulation package called “HAMC” (Hall A Monte Carlo) was used to simulate the events and the spectrometer acceptance. In HAMC, events are generated using a physics class that has information about the cross section and asymmetry. The tracks are generated uniformly in solid angle $d\Omega = \sin(\theta) d\theta d\phi$ and the results later weighted by the differential cross section $\frac{d\sigma}{d\Omega}$. The simulated tracks undergo multiple scattering in the target and energy loss from the target from external and internal Brehmstrahlung as well as ionization loss,

The generated four-vectors are transported to the detector in the HRS focal plane using a set of polynomials that model the trajectories of electrons through the magnetic fields. The beam raster is simulated, which produces a smearing of the beam on target. The events are transported to intermediate apertures such as the collimator or the entrance to quadrupoles. Events that reach the HRS focal plane and intersect the detectors are integrated to compute the total rate and average asymmetry.

The acceptance of the HRS is generally defined by combining the opening geometry of

the intermediate apertures, the nominal settings of which is documented in Ref. (14). In real experiment, however, the edge of the openings are not well defined, as events falling on the edge may correspond to electrons scattering from the aperture's material. Therefore, the real acceptance can be different from the nominal settings. We furtherly fine-tune the HRS acceptance of the simulation in the following way: taking the target variables of good events from data as the starting point, we use the same transport function as in "hamc" to transport these data four-vectors to different apertures, and then read off the edges of the data pattern as the real geometry to define the acceptance. This process is illustrated in Fig. 29.

After the acceptance fine-tuning, the quality of "hamc" is checked by the comparison between simulation results and data on the target variables and kinematics variables. Fig. 30 (Fig. 31) show such comparisons for Left (Right) HRS. The simulation agrees well with data.

2.13 Electromagnetic Radiative Correction

Electrons undergo radiative energy loss such as internal and external Bremsstrahlung and ionization loss, both before and after the scattering. This causes a difference between the kinematics of what we measure at the detector and what really happens at the interaction vertex. Therefore, the measured asymmetry is different from the non-radiated Born asymmetry that we will use for the extraction of C_2 couplings. A radiative correction factor must then be applied to the measured asymmetry, which is calculated as:

$$f = \frac{A(< Q_{det}^2 >, < x_{det}^2 >)}{< A(Q_{vx}^2, x_{vx}^2) >} \quad (33)$$

where $A(< Q_{det}^2 >, < x_{det}^2 >)$ is the asymmetry evaluated at the single kinematics point of mean Q^2 and x measured by the detector, and $< A(Q_{vx}^2, x_{vx}^2) >$ is the averaged asymmetry for all events hitting acceptance, calculated using the vertex kinematics Q_{vx}^2 and x_{vx}^2 .

The radiative correction is performed under the framework of HAMC, where radiative effects are already built in following the treatments first described by Mo & Tsai (28). The

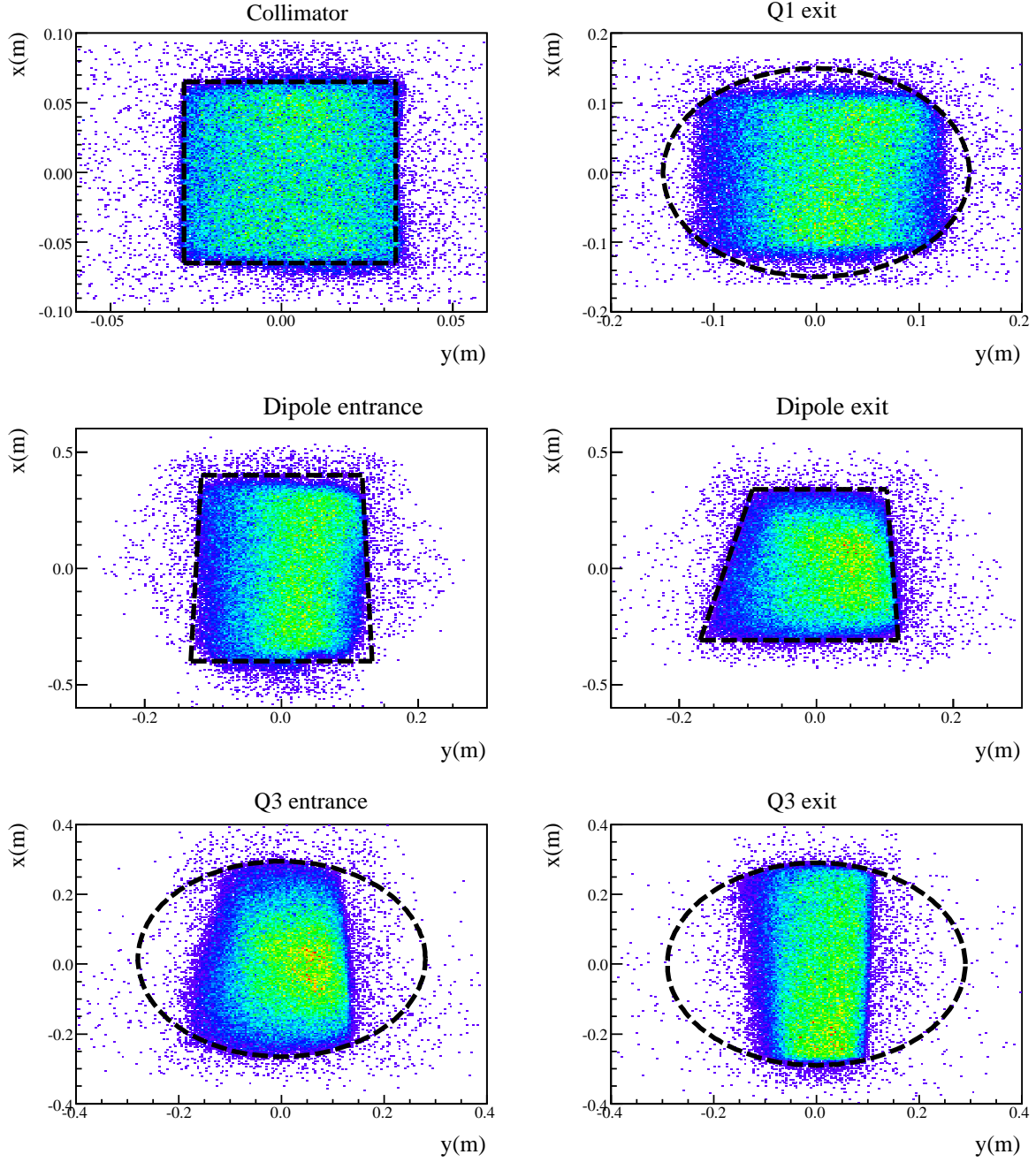


Figure 29: HAMC acceptance tuning. Plotted are the x and y coordinates of data events transported to different apertures. Black lines are the geometry shapes determined according to the data plots, which will be used as acceptance cuts in “hamc”.

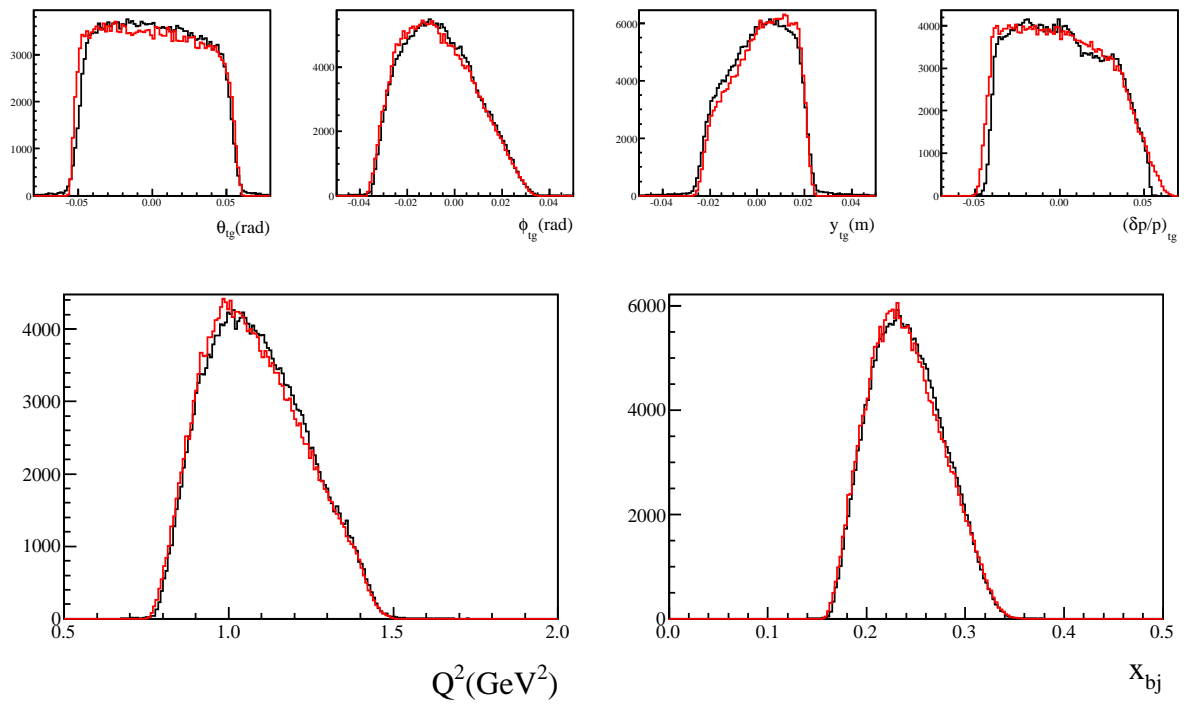


Figure 30: Comparison between HAMC and data for Left HRS kinematics #1.

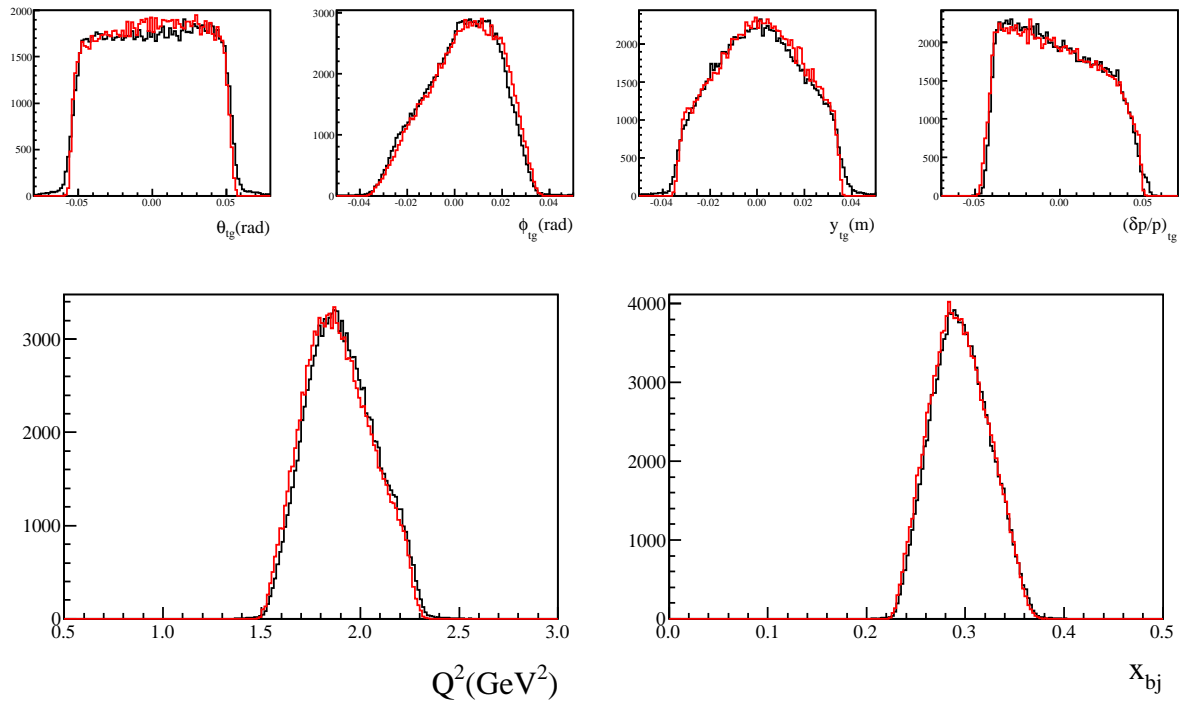


Figure 31: Comparison between HAMC and data for Right HRS kinematics #2.

detailed procedure is described below:

For each event, one starts from the (fixed) beam energy E and a randomly selected scattering angle θ and momentum of the scattered electron E' , where E' is the scattered momentum at the vertex (referred to as E'_v hereafter) but E is not associated with the vertex. The energy loss of incoming and outgoing electrons δE and $\delta E'$ are then calculated using the formula given on page 5-7 of Ref. (29), which includes external bremsstrahlung, internal bremsstrahlung (effective radiator formula), and ionization loss. Then the incoming electron's energy at the vertex is calculated as $E_v = E - \delta E$ and the final momentum of the scattered electron is $E'_d = E' - \delta E'$. If θ and E'_d falls within the spectrometer acceptance, the cross section and the PV asymmetry are calculated using the vertex values E_v and E'_v and are stored. Figure 32 illustrates these definitions:

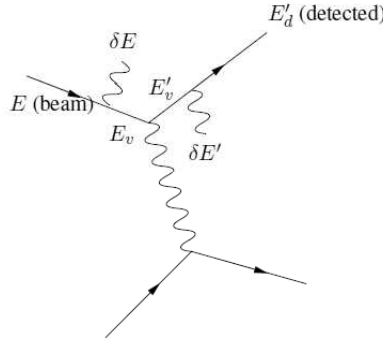


Figure 32: Kinematics used in HAMC to correct the energy loss of incoming and outgoing electrons.

The vertex kinematics (Q^2, W) calculated using (E_v, θ, E'_v) is shown in Fig. 33. As one can see, an event could fall into one of the following categories: $e - {}^2\text{H}$ elastic, quasi-elastic, nucleon resonance, and DIS:

1. For $e - {}^2\text{H}$ elastic, we use code “deut_elastic” from E. Beise (SAMPLE collaboration) (30):

- Cross section is based on parameterization of A and B by J. Ball (31).

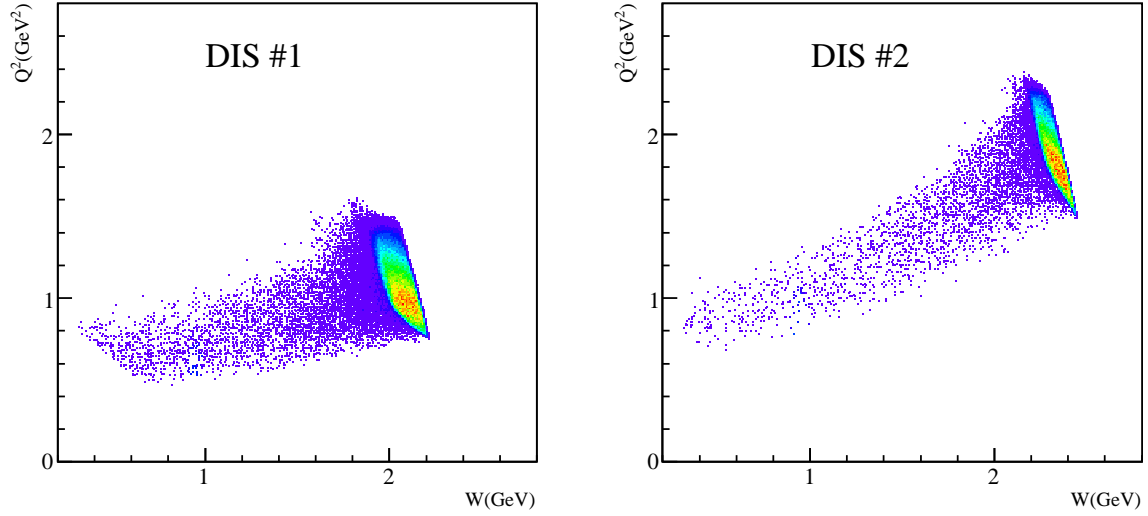


Figure 33: Vertex kinematics range of the two DIS kinematics #1 (left) and #2 (right)

- Asymmetry is based on simple model that compares well to calculation of S. Pollock (32).
- Form factors in the deuteron code are using the J. Kelly parameterization of the nucleon form factors, which worked better for the backward angle measurement of the SAMPLE experiment (30).
- The code gives the deuteron elastic PV asymmetry in the form of $a_0 + a_2 G_M^s$ where G_M is taken to be zero in our calculation.

2. For quasi-elastic:

- Cross section is calculated using the usual elastic formula for the neutron and the proton, then smeared by the smearing algorithm of P. Bosted (extracted from source code of the fit).
- Asymmetry for $e - p$ elastic is calculated using the HAPPEX formula (embedded in

HAMC);

- Asymmetry for $e - n$ elastic is calculated using the same HAPPEX formula as the proton but with the neutron form factors;
- Currently the average of $e - p$ and $e - n$ asymmetries is taken as the quasi-elastic asymmetry. This will be corrected when we are ready for another round of HAMC simulations.

3. For nucleon resonances ($W < 2$):

- Cross section is based on P. Bosted's fits (33);
- Asymmetries are calculated from three models: two “theoretical models” from H. Lee (34) and M. Gorshteyn (35), respectively, and one “toy model” where we used $A_{res} = \frac{\sigma_{res}}{\sigma_{dis}} A_{dis}$ where A_{dis} is calculated from the DIS formula (see below), σ_{dis} is from ??? (NMC fit or also Bosted fit?-XZ), and σ_{res} is from P. Bosted's fit (33);
- The two theoretical models have higher precedence than the “toy model”. Only when the theoretical models don't apply is the “toy model” used.

4. For DIS ($W > 2$):

- The cross section is calculated using Bosted's fits (33);
- The PVDIS asymmetry is calculated using Eqs. (36-38), MSTW2008 NLO (or NNLO) 3-flavor PDFs and quark-parton model formula Eqs. (42), (45), (46), and (47). For R in Eq. (42) again Bosted's fit is used. This is the same prescription as described in the next section for the C_{2q} extraction.

Comments:

The radiative correction is performed under the framework of HAMC, where radiative effects are already built in following the treatments first described by Mo & Tsai (28). Special input to HAMC to customize for this experiment is the information about cross section and asymmetry. Fig ??? shows the vertex kinematics range of events within acceptance. Due to radiation energy loss, a significant fraction of events with lower Q^2 and W would leak into the detector's acceptance. These events may come from all kinds of kinematics regions, including Elastic, Quasi-Elastic and Resonances. Therefore, a complete set of models for cross section and asymmetry calculation, covering the whole kinematics range, are implemented as following:

- Cross section is calculated using the fit over global data from Christy & Bosted [Ref ???], which covers all regions.
- Asymmetries are calculated using different models for different regions:
 - Elastic asymmetry is calculated using ??? (Citing Elizabeth Beise, private comm. or simply SAMPLE?)
 - Quasi Elastic asymmetry is calculated as:

$$A_d = \frac{A_p\sigma_p + A_n\sigma_n}{\sigma_p + \sigma_n} \quad (34)$$

where $\sigma_p(\sigma_n)$ is the proton(neutron) elastic cross section, and $A_p(A_n)$ is the proton(neutron) PVES asymmetry calculated following the standard treatment as G0 [Ref.???] and HAPPEX (6).

- Resonance: Two theoretical calculations from different theorists are used. One is from M. Gorchtein (35). The model cover the whole resonance region upto DIS. Another is from Matusi, Sato and Lee (34). The model is only valid for Δ -resonance

upto $W = 1.4(\text{GeV}/c)$. For higher W , a simple “toy model” that scales the DIS asymmetry by cross section is used:

$$A_{res} = A_{DIS} \times \frac{\sigma_{res}}{\sigma_{DIS}} \quad (35)$$

- DIS asymmetry is calculated according to Eq. 36, with the parton distribution functions obtained from PDF fits provided by the MRST and the CTEQ groups.

Due to the lack of existing measurements of the parity violating asymmetry in the resonance region, the correctness of the theoretical models we used for resonance is not well justified. To better constrain the uncertainty of these models, we took four measurements of resonance kinematics during the experiment. The kinematics coverage were carefully selected so that they could be used for radiative corrections of both DIS kinematics, as shown in Fig. 34 . Table 8 shows the detailed settings together with the measured asymmetry results.

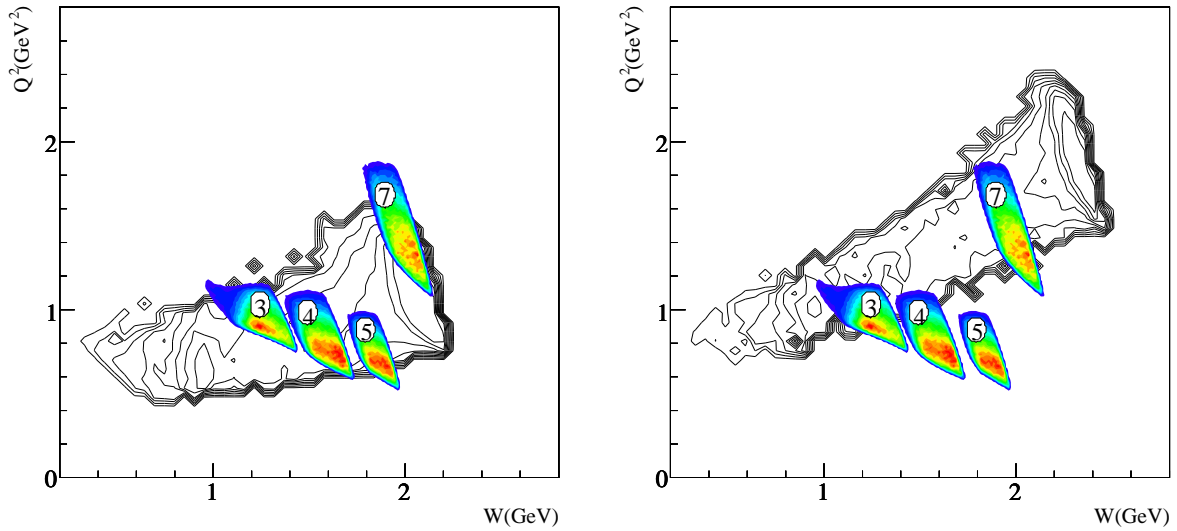


Figure 34: Kinematics coverage of the four resonance measurements, together with the DIS kinematics plotted in black contours.

Comments:

Table 8: Summary of E08-011 Kinematics and Preliminary Asymmetry Results for resonance measurements. The Q^2 and W values are calculated from the central spectrometer settings and we will provide the acceptance- and cross-section average values. We have not corrected the effect of electron energy losses but will do so for the publication. Systematic uncertainties are being analyzed too.

Setting	RES 3	RES 4	RES 5	RES 7
Beam energy E_0 (GeV)	4.8674	4.8674	4.8674	6.0674
Central θ_0	12.9°	12.9°	12.9°	15.0°
Central E'_0 (GeV)	4.0	3.55	3.10	3.66
Central Q^2 (GeV/c) ²	0.983	0.872	0.762	1.513
Central W (GeV/c) ²	1.235	1.575	1.853	1.971
$\langle Q^2 \rangle$ (GeV/c) ²				
$\langle W \rangle$ (GeV)				
A_{PV}^{res} (measured, ppm)	−66.26	−73.4	−60.9	−118.8
Stat. Error (ppm)	7.77	6.9	5.15	16.9

As a check on the theoretical models we used for the resonance, we compare the hamc-calculated asymmetries A_{hamc} with measurement results A_{PV}^{res} for these resonance kinematics. The A_{hamc} is shown in Table 9. Comparing Table 9 and Table 8, the agreement is general good except for RES #3. The difference between A_{hamc} and A_{PV}^{res} , or the statistical uncertainty of A_{PV}^{res} , whichever larger, determines the systematic uncertainty of the theoretical-model calculation of the corresponding kinematics region, which is then used for error estimation of the radiative correction factor.

Model		RES 3	RES 4	RES 5	RES 7
H. Lee	A_{hamc} (ppm)	−82.61	−65.0	−59.1	−117.1
	Syst. Error (rel.)	19%	13%	8.7%	14%
M.Gorshteyn	A_{hamc}	−83.13	−68.2	−61.9	−120.8
	Syst. Error	20%	10%	8.3%	14%

Table 9: Asymmetries calculated by HAMC for the resonance kinematics using different theoretical models.

The radiative correction factor f obtained from the above procedure is shown in Table 10, together with the systematic uncertainties. The physics inputs to “hamc”, the cross-sections and the asymmetry models are all quite precise as confirmed by world data, except for the theoretical models used for resonance asymmetry calculation. Therefore, the systematic uncertainty of f comes mainly from the resonance events contribution. We furtherly divide the resonance region into the following sub-regions according the resonance data we took, and estimate the uncertainty thusly:

- $W^2 < 1.96$: RES 3 locates in this region. This is also where H. Lee’s model is valid. The systematic error of RES 3 (19%) is applied to events in this region.
- $W^2 < 3.0$: RES 4 locates in this region, and its systematic error (13%) is applied to events in this region.
- $W^2 > 3.0$: Both RES 5 and RES 7 locate in this region. The combined systematic error of the two (7.3%) is applied to events in this region.

We choose the results obtained from H. Lee’s model to apply to our DIS data, and use M. Gorshteyn’s model as a cross check.

DIS	Model	$A(< Q_{det}^2 >, < x_{det}^2 >)$ ppm	$< A(Q_{vx}^2, x_{vx}^2) >$ ppm	f	$\Delta f/f$ %
#1	H. Lee	−88.6	−86.8	1.021	2.0
	M. Gorshteyn	−88.6	−87.8	1.009	0.43
#2	H. Lee	−159.6	−156.6	1.019	
	M. Gorshteyn	−159.6	−156.7	1.019	

Table 10: Radiative Correction Factors.

3 Extraction of Quark Axial Charge $2C_{2u} - C_{2d}$

3.1 Formalism and Structure Functions

As shown in Eq.xx, the asymmetry can be written as...

The PV asymmetry of electron deep inelastic scattering (DIS) off a nuclear target is

$$\begin{aligned} A_{PV}^{DIS} &= -\frac{G_F Q^2}{4\sqrt{2}\pi\alpha} \left[2g_A^e Y_1(y) \frac{F_1^{\gamma Z}}{F_1^\gamma} + g_V^e Y_3(y) \frac{F_3^{\gamma Z}}{F_1^\gamma} \right] \\ &= -\frac{G_F Q^2}{4\sqrt{2}\pi\alpha} [a_1(x) Y_1(y) + a_3(x) Y_3(y)] , \end{aligned} \quad (36)$$

where G_F is the Fermi constant, α is the fine structure constant, x is the Bjorken scaling variable, $y = \nu/E$ is the fractional energy loss of the electron with E the incident electron energy. With $r^2 = 1 + \frac{Q^2}{\nu^2}$ and $R^{\gamma, \gamma Z}$ the ratio of the longitudinal and transverse virtual photon electromagnetic absorption and the $\gamma - Z^0$ interference cross sections, respectively:

$$Y_1 = \left[\frac{1 + R^{\gamma Z}}{1 + R^\gamma} \right] \frac{1 + (1-y)^2 - y^2 \left[1 - \frac{r^2}{1+R^{\gamma Z}} \right] - xy \frac{M}{E}}{1 + (1-y)^2 - y^2 \left[1 - \frac{r^2}{1+R^\gamma} \right] - xy \frac{M}{E}} \quad (37)$$

and

$$Y_3 = \left[\frac{r^2}{1 + R^\gamma} \right] \frac{1 - (1-y)^2}{1 + (1-y)^2 - y^2 \left[1 - \frac{r^2}{1+R^\gamma} \right] - xy \frac{M}{E}} . \quad (38)$$

To a good approximation one has $R^\gamma \approx R^{\gamma Z}$ and $Y_1(y) \approx 1$.

The $a_{1,3}$ terms are related to the $F_{1,3}$ structure functions as

$$a_1(x) = 2g_A^e \frac{F_1^{\gamma Z}}{F_1^\gamma} , \quad (39)$$

$$a_3(x) = g_V^e \frac{F_3^{\gamma Z}}{F_1^\gamma} . \quad (40)$$

However, since the convention of most parameterizations is to fit the structure function F_2 and R simultaneously to cross section data, it is more appropriate to use F_2 which are related to F_1 as:

$$F_2 = \frac{2xF_1(1+R)}{r^2} \quad (41)$$

or

$$F_1 = \frac{r^2 F_2}{2x(1+R)}. \quad (42)$$

In the extraction of $C_{1,2}$ one must evaluate all structure functions from world parameterizations of cross section data, which can be done at the QCD LO, NLO, or higher orders. But the simple quark parton model (QPM) provides a simple and more intuitive view for the structure functions: In the QPM these can be constructed from parton distribution functions (PDF) $q_i(x)$ and $\bar{q}_i(x)$:

$$F_1^\gamma(x) = \frac{1}{2} \sum Q_i^2 [q_i(x) + \bar{q}_i(x)], \quad (43)$$

$$F_1^{\gamma Z}(x) = \sum Q_i g_V^i [q_i(x) + \bar{q}_i(x)], \quad (44)$$

$$F_3^{\gamma Z}(x) = 2 \sum Q_i g_A^i [q_i(x) - \bar{q}_i(x)], \quad (45)$$

$$F_2^\gamma(x) = 2x F_1^\gamma(x) = x \sum Q_i^2 [q_i(x) + \bar{q}_i(x)] \quad (46)$$

$$F_2^{\gamma Z}(x) = 2x F_1^{\gamma Z}(x) = 2x \sum Q_i g_V^i [q_i(x) + \bar{q}_i(x)] \quad (47)$$

where the summation is over the quark flavor $i = u, d, s \dots$, Q_i is the corresponding quark electric charge, and R is assumed to be zero in the QPM. Defining $q_i^\pm(x) \equiv q_i(x) \pm \bar{q}_i(x)$, one has

$$a_1(x) = 2 \frac{\sum C_{1i} Q_i q_i^+(x)}{\sum Q_i^2 q_i^+(x)}, \quad (48)$$

$$a_3(x) = 2 \frac{\sum C_{2i} Q_i q_i^-(x)}{\sum Q_i^2 q_i^-(x)}, \quad (49)$$

For an isoscalar target such as the deuteron, neglecting effects from heavier quark flavors and assuming the isospin symmetry that $u^p = d^n$, $d^p = u^n$ [$u, d^{p(n)}$ are the up and down quark PDF in the proton (neutron)], $s = \bar{s}$, and $c = \bar{c}$, the functions $a_{1,3}(x)$ simplify to

$$a_1(x) = \frac{6 [2C_{1u}(1+R_c) - C_{1d}(1+R_s)]}{5 + R_s + 4R_c}, \quad (50)$$

$$a_3(x) = \frac{6 (2C_{2u} - C_{2d}) R_v}{5 + R_s + 4R_c}, \quad (51)$$

where $R_c \equiv [2(c + \bar{c})]/(u + \bar{u} + d + \bar{d})$, $R_s \equiv [2(s + \bar{s})]/(u + \bar{u} + d + \bar{d})$ and $R_V \equiv (u - \bar{u} + d - \bar{d})/(u + \bar{u} + d + \bar{d})$.

To estimate the uncertainty due to structure function parameterizations, it is useful to evaluate the value of $a_{1,3}$ assuming that the nucleon is simply made of valence u and d quarks. For the deuteron this results in $u^+ = d^+ = u^- = d^-$, $s = c = 0$, which lead to the expressions in PDG2012 (36):

$$a_1(x) = \frac{6}{5} (2C_{1u} - C_{1d}) , \quad (52)$$

$$a_3(x) = \frac{6}{5} (2C_{2u} - C_{2d}) , \quad (53)$$

i.e., no structure function or parton distribution function is involved. These will be referred to as the “no structure” values hereafter. Values of $a_{1,3}$ using different PDF fits are presented in Sec. 3.3 and the difference from these no-structure values will be used to estimate the maximal uncertainty due to structure functions.

3.2 Radiative Corrections

In this section the effect of higher order Feynman diagrams will be discussed. This includes the “running” of all coupling constants involved due to vacuum polarization or loop diagrams, as well as the effect of the box diagrams of two-boson exchanges. The internal corrections such as vertex corrections and internal bremsstrahlung, as well as external corrections due to the energy loss of incoming and outgoing electrons were discussed in section ??? and will not be included here.

3.2.1 Running of all coupling constants

1. The α_{EM} is evaluated at our measured Q^2 from $\alpha_{EM}|_{Q^2=0} = 1/137.036$ (36). This takes into account purely EM vacuum polarization, which cannot be corrected otherwise.

2. The Fermi constant is $G_F = 1.1663787(6) \times 10^{-5} \text{ GeV}^{-2}$ (36).
3. The value of $\sin^2 \theta_W$ and its running does not go directly into the asymmetry calculation;
4. The $C_{1,2}^{u,d}$ are evaluated at our measured Q^2 in the \overline{MS} scheme using a fixed Higgs mass $M_H = 124.5 \text{ GeV}$ and the rest of the parameters determined by the global fit (37). This calculation includes the “charge radius effect” and a preliminary estimate of the interference between γ -exchange and γZ box.
 - K. Kumar commented it seems to include all EW RC, plus a preliminary estimation of the interference between γ -exchange and γZ box.
 - Minor tweaks might need to be done for the $\gamma - (\gamma Z)$ term.

The exact values are shown below. The definition of all parameters can be found in PDG2012, and their values can be compared to Table 10.2 of PDG2012 (36) which defines them at $Q^2 = 0$ and is more valid for lower energies (such as Atomic PV) than PVDIS.

5. Interference between Z -exchange and $\gamma\gamma$ box is NOT calculated anywhere, although it is estimated to be the same order as the $\gamma - (\gamma Z)$ interference.
6. Effects of the $\gamma\gamma$ box, which should go into the denominator of Eq. (36) (Andrei A., hep-ph/0502128), is NOT calculated anywhere.
7. Additional EM radiative corrections, such as vertex and (some?) loop corrections still need to be studied, see next section.

Table 11: Values of $C_{1,2q}$ calculated at our measured Q^2 values using the best fit of the Higgs mass $m_H = 102$ GeV.

Q^2 (GeV/c) ²	1.901	1.085
ρ'	0.9891	0.9891
ρ	1.0007	1.0007
κ'	0.9943	0.9958
κ	1.0298	1.0298
λ'	-1.8×10^{-5}	-1.8×10^{-5}
λ_{2u}	-0.0110	-0.0104
λ_{2d}	0.0006	0.0008
C_{1u}	-0.1913	-0.1908
C_{1d}	0.3429	0.3427
C_{2u}	-0.0388	-0.0382
C_{2d}	0.0284	0.0280
$2C_{1u} - C_{1d}$	-0.7255	-0.7244
$2C_{2u} - C_{2d}$	-0.1061	-0.1045

3.2.2 Box corrections

In the one-boson exchange (OBE) picture, the parity-violating asymmetry A_{PV}^0 is proportional to the interference between γ and Z exchange amplitudes:

$$A_{PV}^0 = \frac{\sigma^+ - \sigma^-}{\sigma^+ + \sigma^-} \approx \frac{2\text{Re}(M_\gamma^* M_Z)}{|M_\gamma|^2}, \quad (54)$$

where only the parity-violating part of M_Z is retained.

The correction to the PV cross section arising from the $\gamma\gamma$ and γZ two-boson exchange (TBE) contributions can be obtained from Eq. 54 by the replacements

$$M_\gamma \rightarrow M_\gamma + M_{\gamma\gamma}, \quad (55)$$

$$M_Z \rightarrow M_Z + M_{\gamma Z} + M_{Z\gamma}. \quad (56)$$

There are three types of corrections arising from the interference of the OBE (γ or Z) and TBE ($\gamma\gamma$ or γZ) amplitudes (the so-called box diagrams), which we will denote as $\gamma(\gamma Z)$, $Z(\gamma\gamma)$,

and $\gamma(\gamma\gamma)$. The first is an electroweak correction whereas the last two are electromagnetic corrections. These corrections can be identified as

$$\delta_{\gamma(\gamma Z)} = \frac{2\text{Re}(M_\gamma^* M_{\gamma Z} + M_\gamma^* M_{Z\gamma})}{2\text{Re}(M_\gamma^* M_Z)}, \quad (57)$$

$$\delta_{Z(\gamma\gamma)} = \frac{2\text{Re}(M_Z^* M_{\gamma\gamma})}{2\text{Re}(M_Z^* M_\gamma)}, \quad (58)$$

$$\delta_{\gamma(\gamma\gamma)} = \frac{2\text{Re}(M_\gamma^* M_{\gamma\gamma})}{|M_\gamma|^2}. \quad (59)$$

The correction to the Born-level PV asymmetry A_{PV}^0 can be represented as

$$A_{PV} = (1 + \delta_{box})A_{PV}^0 \equiv \left(\frac{1 + \delta_{Z(\gamma\gamma)} + \delta_{\gamma(\gamma Z)}}{1 + \delta_{\gamma(\gamma\gamma)}} \right) A_{PV}^0, \quad (60)$$

where A_{PV} is the full asymmetry including TBE corrections. Since the electromagnetic TBE correction $\delta_{\gamma(\gamma\gamma)}$ is typically only a few percent, the full correction δ_{box} can be written approximately as

$$\delta_{box} \approx \delta_{Z(\gamma\gamma)} + \delta_{\gamma(\gamma Z)} - \delta_{\gamma(\gamma\gamma)}. \quad (61)$$

There is a great deal of cancellation among these three terms, in particular for the vector part of the Z -nucleon coupling, which is related to the γ -nucleon coupling by an isospin rotation. There are also infra-red (IR) divergences that cancel exactly.

The soft-photon exchange contribution to δ_{box} , which contains the IR divergences, can be separated out from the hard photon exchange contribution which is relevant for DIS kinematics. The soft photon contribution involves the nucleon as a whole. This is the usual Mo-Tsai correction that is independent of nucleon structure. Therefore only the hard photon contribution needs to be considered. For Q^2 in the range $1 - 2 \text{ GeV}^2$, the hard photon contribution of the TPE correction $\delta_{\gamma(\gamma\gamma)}$ for scattering from the weighted sum of incoherent quarks $2u + d$ is positive, and of order $0 - 2\%$, depending on the specific kinematics. The total δ_{box} for the same incoherent sum is positive and of order $0 - 1\%$.

3.3 Extracting C_{2q}

To extract $2C_{2u} - C_{2d}$ from the measured asymmetry, we first calculate the $F_1^{\gamma Z}$ contribution of Eq. (36) assuming the standard model values for C_{1q} , then subtract it from the measured asymmetry to obtain the measured $F_3^{\gamma Z}$ contribution. The measured $F_3^{\gamma Z}$ contribution is compared with the calculated value to obtain $2C_{2u} - C_{2d}$. During this procedure both the QED and the electroweak radiative corrections must be properly taken into account as described in the previous section. The non-perturbative QCD effect which was not accounted for in the structure function calculations is not included here, but will be discussed in the next section.

The inputs to the calculations of the $F_1^{\gamma Z}$ and $F_3^{\gamma Z}$ contributions to Eq. (36) are described below:

1. Calculation of structure functions based on “PDF combined with QPM”: For the structure functions in Eqs. (48-49) the best evaluation is performed at the QCD NLO or N²LO level. However, except for the CTEQ/JLab (“CJ”) fit, which is NLO, almost all parameterizations available do not provide calculation for the Z –exchange or $\gamma - Z$ interference terms $F_{1,3}^{\gamma Z}$. The CJ fit, on the other hand, does not apply to Q^2 below 1.7 (GeV/c)^2 and would not work for the measured $Q^2 = 1.085 \text{ (GeV/c)}^2$ data. Therefore the simple parton model, Eqs. (45-47) are used to construct structure functions. The PDF fits used in this “PDF-QPM combination” include CTEQ10 (38, 39) and MSTW2008 (40, 41), and results at the $Q^2 = 1.901 \text{ (GeV/c)}^2$ are compared with the full NLO CJ fit to study the sensitivity to the PDF used.
2. Once values for F_2^γ and $F_2^{\gamma Z}$ are obtained, Eq. (42) is used to calculate F_1^γ and $F_1^{\gamma Z}$ where the latest experimental fit of R (33) is used.
3. Effect of possible difference between $R^{\gamma Z}$ and R^γ were studied (42) : To account for a shift of 1 ppm in the asymmetry, 7.7% and 4.5% differences between $R^{\gamma Z}$ and R^γ are

needed, for $Q^2 = 1.085$ and 1.901 (GeV/c^2), respectively. This uncertainty is not included in the current calculation for the asymmetry shown in Table 12.

4. Once the appropriate a_1 and a_3 terms for the asymmetry are evaluated, we compare them to our measured asymmetry and extract C_{2q} as:

$$[2C_{2u} - C_{2d}] (\text{measured}) = [2C_{2u} - C_{2d}]^{SM \text{ value}} \times \frac{A_{PV}^{\text{measured}} - A_{a_1 \text{ term}}^{\text{calculated}}}{A_{a_3 \text{ term}}^{\text{calculated}}} \quad (62)$$

Table 12 summarizes our calculation of the SM value for the asymmetry.

Table 12: Comparison of asymmetry calculation using different structure functions. The value for $\alpha_{EM}(Q^2)$ (run from $1/137.036$ at $Q^2 = 0$) and $C_{1,2}^{u,d}(Q^2)$ are also shown.

	$\langle Q^2 \rangle = 1.085, \langle x \rangle = 0.241$	$\langle Q^2 \rangle = 1.901, \langle x \rangle = 0.295$
Physical couplings		
$\alpha_{EM}(Q^2)$	1/134.45	1/134.20
C_1^u, C_1^d	-0.19059, 0.34257	-0.1913, 0.3429
$2C_{1u} - C_{1d}$	-0.72375	-0.7255
C_2^u, C_2^d	-0.03827, 0.02802	-0.0388, 0.0284
$2C_2^d - C_2^u$	-0.10456	-0.1060
$A(a_1), A(a_3)$ terms in ppm		
“no structure”	-83.21, -5.57	-145.77, -14.56
CTEQ/JLab (CJ) full fit	NA	-147.86, -13.60
“PDF+QPM” MSTW2008 LO	-83.75, -4.598	-146.71, -13.10
“PDF+QPM” MSTW2008 NLO	-84.39, -4.735	-147.22, -13.39
“PDF+QPM” MSTW2008 NNLO	-84.41, -4.774	-147.17, -13.48

As one can see from the table above, the MSTW 2008 NLO PDF combined with QPM gives the closest values to the full CJ fit at $Q^2 = 1.901$ (GeV/c^2). In order to utilize the measured asymmetries at both $Q^2 = 1.085$ and 1.901 (GeV/c^2), the MSTW NLO combined with QPM values will be used.

Our final result on $2C_{2u} - C_{2d}$, extracted from the $Q^2 = 1.901$ (GeV/c^2) asymmetry data, is

$$2C_{2u} - C_{2d} = xxx \pm 0.052(\text{total}) \quad (63)$$

(cite stat, syst, model separately!) this is to be compared with the Standard Model prediction -0.1060 at this Q^2 or the current PDG2012 best estimate $\dots \pm 0.24$. To compare with previous world data, the first PVDIS data from SLAC should be re-analyzed on a equal footing, i.e., an extraction of $2C_{2u} - C_{2d}$ with the value of the quark weak vector charge term $2C_{1u} - C_{1d}$ fixed to the SM. The reanalysis of the SLAC data gives $(2C_{2u} - C_{2d})_{SLAC} = -0.17 \pm 0.30$.

To allow extraction of $2C_{2u} - C_{2d}$ from both Q^2 points, the higher twist effect must be taken into account properly. This is discussed in the next section and a simultaneous fit to the higher twist effect and $2C_{2u} - C_{2d}$ will be performed.

3.4 The Higher Twist Effect and a Simultaneous Fit to the Higher Twist Coefficient β_{HT} and $2C_{2u} - C_{2d}$

The higher twist effects refer to the interaction between quarks inside the nucleon at low Q^2 , where renormalization of the QCD coupling breaks down. At a relative low Q^2 but not low enough for the effective QCD coupling to diverge, the higher twist effects introduce a $1/Q^2$ -dependence to the structure functions in addition to the $\ln Q^2$ perturbative QCD evolution. The higher twist effects on R^γ were estimated in Ref. (43) and the effect on the asymmetry is negligible. Previous data on the higher twist effect of electroweak structure functions $F_{1,3}^{\gamma Z}$ are scarce, and the only data that can be directly applied to $F_3^{\gamma Z}$ here are from the neutrino structure function H_3^ν (43). If applying the observed H_3^ν higher twist Q^2 dependence to $F^3 \gamma Z$ alone, one expects the asymmetry to shift by $+0.70$ ppm and $+1.2$ ppm for the lower and the higher Q^2 results, a less than 1% effect. However, since the non-perturbative interaction between quarks inside the nucleon should not depend on the boson (photon or Z^0) exchanged between the quark and the incident electron, one expects a large, if not complete, cancellation between $F^{1,3 \gamma Z}$ and F_1^γ , i.e. the numerator and the denominator of both a_1 and a_3 terms. The PVDIS asymmetry should therefore have very small higher twist effect.

The higher twist effect to PVDIS can be investigated through a simultaneous fit to the higher twist coefficient β_{HT} and $2C_{2u} - C_{2d}$. The antazi

$$A_{PV} = A_{PV}^{EW} \left(1 + \frac{\beta_{HT}}{(1-x)^3 Q^2} \right) \quad (64)$$

where A_{PV}^{EW} is the value calculated from Eq. 36 and β_{HT} is the higher twist coefficient. Our results are...

4 Summary

References and Notes

- 1.
2. R. Michaels, P.E. Reimer, X. Zheng et al., Jefferson Lab E08-011, $\vec{e}-^2\text{H}$ Parity Violating Deep Inelastic Scattering (PVDIS) at CEBAF 6 GeV.
3. C.Y. Prescott *et al.*, Phys. Lett. **B77** (1978) 347; C.Y. Prescott *et al.*, Phys. Lett. **B84** (1979) 524
4. P.A. Souder *et al.* Phys. Rev. Lett. **65** 694 (1990).
5. R. D. McKeown, Phys. Lett. B **219** (1989) 140.; D.T. Spayde, *et al.* Phys. Lett. **B583** (2004) 79; T. Ito, *et al.* Phys. Rev. Lett. **92** (2004) 102003.
6. K.A. Aniol *et al.*, Phys. Lett. B **509** (2001) 211; K.A. Aniol *et al.*, Phys. Rev. **C69** (2004) 065501; K.A. Aniol *et al.*, Phys. Rev. Lett. **96** (2006) 022003; K.A. Aniol *et al.*, Phys. Lett. **B635** (2006) 275; A. Acha *et al.*, Phys. Rev. Lett. **98** (2007) 032301. Z. Ahmed *et al.*, arXiv:1107.0913 [nucl-ex].
7. D.H. Beck, Phys. Rev. D **39** (1989) 3248; D.S. Armstrong *et al.*, Phys. Rev. Lett. **95** (2005) 092001; D. Androic *et al.*, Phys. Rev. Lett. **104** (2010) 012001.

8. S. Abrahamyan, *et al.* Phys. Rev. Lett. **108**, 112502 (2012); C.J. Horowitz, *et al.* Phys. Rev. C **85**, 032501(R) (2012).
9. R. Subedi *et al.* publication submitted to NIM.
10. C. K. Sinclair, *et al.* Phys. Rev. ST Accel. Beams **10**, 023501 (2007); J. Hansknecht, *et al.* Phys. Rev. ST Accel. Beams **13**, 010101 (2010).
11. K. D. Paschke, Eur. Phys. J. A **32**, 549 (2007).
12. J. Grames, *et al.*, “Two Wien Filter Spin Flipper” in Proceedings of the 2011 Particle Accelerator Conference, New York, New York (2011).
13. W. Barry, NIM A301 (1991) 407; T. Powers, L. Doolittle, R. Ursic, and J. Wagner, Proc. 7th Workshop on Beam Instrumentation, AIP Conf.Proc. **390**, Ed. A.. Lumpkin and C.E. Eyberger (1997); JLAB-TN-96-021.
14. J. Alcorn *et al.*, Nucl. Instrum. Meth. A **522**, 294 (2004).
15. W.A. Watson *et al.*, CODA: A Scalable, Distributed Data Acquisition System, in Proc. of the Real Time 1993 Conference, p. 296; G. Heyes *et al.*, The CEBAF Online Data Acquisition System, in Proc. of the CHEP Conference, 1994, p. 122; D.J. Abbott *et al.*, CODA Performance in the Real World, 11th IEEE NPSS Real Time 199 Conference, JLab-TN-99-12 (1999).
- 16.
17. C.K. Sinclair, “Electron Beam Polarimetry”, Tech Note JLAB-ACC-98-04; T.J. Gay and F.B. Dunning, Rev. Sci. Instrum. **63** (1992) 1635; T.J. Gay *et al.*, Rev. Sci. Instrum. **63** (1992) 114. S. Mayer *et al.*, Rev. Sci. Instrum. **64** (1993) 952.

- 18.
- 19.
- 20.
- 21.
- 22.
23. A. Acha *et al.* [HAPPEX Collaboration], Phys. Rev. Lett. **98**, 032301 (2007) [nucl-ex/0609002].
24. K. A. Aniol *et al.* [HAPPEX Collaboration], Phys. Rev. Lett. **96**, 022003 (2006) [nucl-ex/0506010].
- 25.
26. A. Afanasev, priv. communication.
27. M. Seely, *Gas Chromatograph Analysis for Deuterium Sample*, July 26, 2002.
28. L. W. Mo and Y. -S. Tsai, Rev. Mod. Phys. **41**, 205 (1969).
29. R. Michaels, Formulas for Hall A Monte Carlo (2008), URL: http://hallaweb.jlab.org/parity/prex/hamc/hamc_formulas.pdf
30. E. J. Beise, M. L. Pitt and D. T. Spayde, Prog. Part. Nucl. Phys. **54**, 289 (2005) [nucl-ex/0412054].
31. D. Abbott *et al.* [JLAB t20 Collaboration], Eur. Phys. J. A **7**, 421 (2000) [nucl-ex/0002003].
32. S. J. Pollock, Phys. Rev. D **42**, 3010 (1990) [Erratum-ibid. D **43**, 2447 (1991)].

33. P. E. Bosted and M. E. Christy, Phys. Rev. C **77**, 065206 (2008) [arXiv:0711.0159 [hep-ph]].
34. K. Matsui, T. Sato and T. -S. H. Lee, Phys. Rev. C **72**, 025204 (2005) [nucl-th/0504051].
35. M. Gorchtein, C. J. Horowitz and M. J. Ramsey-Musolf, Phys. Rev. C **84**, 015502 (2011) [arXiv:1102.3910 [nucl-th]].
36. J. Beringer et al. (Particle Data Group), Phys. Rev. D **86**, 010001 (2012).
37. J. Erler, priv. communication.
38. J. Pumplin, D. R. Stump, J. Huston, H. L. Lai, P. M. Nadolsky and W. K. Tung, JHEP **0207**, 012 (2002) [hep-ph/0201195].
39. H. -L. Lai, M. Guzzi, J. Huston, Z. Li, P. M. Nadolsky, J. Pumplin and C. -P. Yuan, Phys. Rev. D **82**, 074024 (2010) [arXiv:1007.2241 [hep-ph]].
40. A. D. Martin, W. J. Stirling, R. S. Thorne and G. Watt, Phys. Lett. B **652**, 292 (2007) [arXiv:0706.0459 [hep-ph]].
41. A. D. Martin, W. J. Stirling, R. S. Thorne and G. Watt, Eur. Phys. J. C **63**, 189 (2009) [arXiv:0901.0002 [hep-ph]].
42. T. Hobbs and W. Melnitchouk, Phys. Rev. D **77**, 114023 (2008) [arXiv:0801.4791 [hep-ph]].
43. S. Alekhin, S. A. Kulagin and R. Petti, AIP Conf. Proc. **967**, 215 (2007) [arXiv:0710.0124 [hep-ph]].
44. F.E. Maas *et al.*, Phys. Rev. Lett. **93** (2004) 022002; F.E. Maas *et al.*, Phys. Rev. Lett. **94** (2005) 152001; S. Baunack *et al.*, Phys. Rev. Lett. **102** (2009) 151803.

45. We would like to thank the personnel of Jefferson Lab for their efforts which resulted in the successful completion of the experiment. We thank T.-S.H. Lee, M. Gorshteyn, P. Blunden, A. Afanasev, J. Erler and their collaborators for carrying out the calculations used in this publication (list all theorists not co-author-ed here). X. Zheng would like to thank the Medium Energy Physics Group at the Argonne National Lab for supporting her during the initial work of this experiment. This work was supported by the Department of Energy (DOE), the National Science Foundation, and the Jeffress Memorial Trust. Jefferson Science Associates, LLC, operates Jefferson Lab for the U.S. DOE under U.S. DOE contract DE-AC05-06OR23177.